ORIGINAL ARTICLE

Modeling, simulation, and validation of a TB41 crash test of the H2/W5/B concrete vehicle restraint system

Ł. Pachocki[1] · D. Bruski[1]

Abstract

The paper addresses numerical simulations of a concrete vehicle restraint system. The model is described in detail. The advanced material law of the continuous surface cap model was used to analyze the damage locations in concrete barrier segments. The results were validated against the TB41 full-scale crash test. The test was conducted in compliance with European standard EN 1317, and the validation was performed in accordance with the PD CEN/TR 16303 technical report. The force and moment envelopes of the road safety barrier during a vehicle crash are provided. The detailed concrete segment model successfully reproduced the characteristic splitting failure cracks that were found near the connection of the adjacent barrier segments in the actual structure after the full-scale crash test.

1 Introduction

Every year, approximately 1.35 million people die in traffic crashes around the world [1]. With the continuing development of road networks and the increasing number of vehicles in operation, it is necessary to make all possible efforts to reduce the number of accidents. However, when a vehicle crash does occur, safety barriers are devices installed on roads to reduce the negative effects of such events. As Budzyński et al. [2, 3] points out, if used correctly, in justified places, these devices may enhance road safety. However, this leads to the need for the development of new methods for selecting optimal road restraint systems [4]. To quantify the classes of specific designs, normalized measures must be provided for every barrier used on European roads. This will help to maintain a constant flow of feedback, which will enable the production of continuously improving road safety equipment. In Europe, road safety barriers are tested in compliance with the EN 1317 standard [5, 6].

There are multiple road safety barrier designs. Most of them are made of steel; however, in some places, concrete systems may be more suitable. Concrete barriers are generally rigid structures. The quality of the concrete need to be controlled during the production stage, e.g., using numerical methods to predict the strength development as a function of the concrete hardening temperature [7]. Concrete road safety barriers are mostly used where the free space behind the barrier is small or when the risk of a vehicle going through the barrier must be reduced, e.g., on overpasses and bridge piers. On the other hand, concrete barriers may exert significant forces on the occupants of a vehicle during an accident [8]. Thus, an appropriate balance between construction and occupant safety must be preserved. A general overview concerning concrete barriers was presented in Ref. [9].

Numerical simulations of vehicle impact phenomena are often performed in a finite element method (FEM) environment using an explicit scheme to integrate the equations of motion. Generally, simulations may be a valuable tool for this type of analysis. Compared with experimental crash testing, simulations make the testing of different types of barriers and vehicles possible on a much larger scale. This factor becomes crucial in the case of continuous development of the vehicle fleet (e.g., the emergence of new electric engine designs). There are a number of publications confirming the reliability and usefulness of FEM simulations in the field of road traffic safety. The most commonly used software for numerical calculations is LS-DYNA. Numerical simulations of crash tests began in the early 1990s. Most likely, as suggested in [10], the first publication in which nonlinear dynamic finite element analysis (FEA) in roadside

✉ Ł. Pachocki
lukasz.pachocki@pg.edu.pl

1   Department of Mechanics of Materials and Structures,
     Faculty of Civil and Environmental Engineering, Gdańsk
     University of Technology, ul. Narutowicza 11/12,
     80-233 Gdańsk, Poland

safety was utilized was a study by Wekezer et al. published in 1993 [11]. That paper concerns an impact simulation of a car with a light pole. Since then, numerous studies have been published in which numerical simulations were used to analyze vehicle impacts. Most of them concern steel barriers; nevertheless, all types of road safety equipment have been analyzed, including concrete barriers. Wekezer et al. [12] evaluated the crashworthiness of Florida beam-and-post concrete bridge barriers. The results revealed serious snagging problems. The authors proposed a retrofit design for the analyzed barriers that resulted in a reduction of the acceleration peaks by approximately 50%. The paper contributed to a better understanding of barrier performance. Bonin et al. [13] proposed modifications to an existing concrete barrier system used in Italy. The modifications involved shortening the length of each barrier segment and using lightweight concrete. This modified design was evaluated through numerical simulations, and the results showed an improvement in impact severity; however, the safety system had a tendency to cause vehicle rollover, and the authors suggested that the cross-sectional shape should be studied to address this issue. Ren et al. [14] conducted one of the first numerical simulations with steel road safety barriers. The results were compared with a full-scale crash test and proved the correctness of the computational model. Then, Borovinšek et al. [15] expanded the previous research by modeling the safety barrier reinforcements to determine the best barrier design for high containment level. Itoh et al. [16] investigated collisions of heavy trucks with concrete barriers. A numerical simulation was compared with a full-scale crash test. The research showed that after the front of the truck first impacted the barrier, the barrier contained the truck and started redirecting it back. Then, a second collision occurred when the rear of the truck impacted the restraint system, which resulted in larger displacements of the barrier than those in the first front collision. The authors highlighted that the simulation could replicate a real collision and that the results could be used to analyze the behavior of trucks as well as concrete barriers during impacts. Borkowski et al. [17, 18] conducted a series of numerical tests to examine the behavior of a concrete barrier. The results presented in [17] indicated that the impact angle has a strong effect on the safety of the vehicle occupants as well as on the motion trajectory of the vehicle after the collision. In paper [18], two types of concrete barriers were examined: a portable barrier and a rigid barrier fixed to the road surface. The results indicated a substantial influence of the barrier installation method on the collision course and the dynamic loads affecting the vehicle occupants. Wang et al. [19], based on previous cable barrier research, presented a methodology to create an efficient FE model for cable barriers. In 2015, Li et al. [20] applied the 50th percentile male Hybrid III crash test dummy to investigate its behavior during the vehicle crash

against road safety barriers. The authors found the potential danger of dummy's head hitting the side window during the crash with stiff barriers, e.g., those made of concrete. Abraham et al. [21] assessed the distributions of the impact angle and velocity in run-off-road accidents and conducted simulations to evaluate the normal containment level of concrete barriers in nonstandard collisions. The results of the FE simulations indicated a significant increase in the Acceleration Severity Index (ASI) value with increasing impact angle and impact velocity. In the years 2016 and 2018 Klasztorny et al. [22, 23] presented results of modeling and validation of the steel road safety barrier. The novelty of the authors' approach was characterized by installing the barrier on the horizontal concave road arch. Moreover, the authors investigated the influence of the specifically designed composite overlay on impact severity indices. Mohan et al. [24] examined the connections of concrete barriers and the behavior of the concrete, including its failure. The numerical results showed good correlations with the results of full-scale crash tests. Some papers have also considered optimization methods to enhance road barrier designs. Yin et al. [25] used radial basis function-based metamodeling approach to perform design optimization for a concrete barrier. Later, in 2017, Yin et al. [26] used similar methodology to optimize the design of a new steel W-beam guardrail so as to solve the tire snagging issue. Wang et al. [27] used a combination of metamodeling- and probability-based approach to assess the probabilities of exceedance and/or failure for concrete median barriers. Some researchers also used the parametric studies to investigate the influence of selected factors, e.g., Wilde et al. [28], basing on numerical simulations of the TB51 crash test against a bridge barrier, found that the curb-to-barrier distance has little impact on the working width of the barrier. In 2012, requirements for numerical simulations have been proposed and standardized in the PD CEN/TR 16303 technical reports [29–32]. This standardization has significantly increased the importance of simulations and lowered the costs of developing and testing vehicle restraint systems (VRSs).

This work aims to present numerical simulations validated against the results from a full-scale TB41 crash test [6] of the H2/W5/B concrete barrier. The test parameters are as follows: A 10 t heavy goods vehicle (HGV) hits a concrete barrier with a speed of 70 km/h and at an angle of 8°. The other objectives are to provide an overview of the damage and to determine the forces acting on the barrier during the crash test. Next, a numerical analysis of an isolated concrete segment loaded with the forces extracted from the 10 t truck impact simulation will be presented. Detailed model analysis allows the splitting failure of the concrete to be observed. The splitting failure and its numerical modeling have been already presented by, e.g., Gálvez et al. [33]. Later, Rucka and Wilde

[34] studied the monitoring of specific patterns of damage evolution in reinforced concrete. Those papers helped in a broader understanding of this complex phenomenon. Hence, they allowed the comparison of the numerical simulation results with the damage locations in the actual object from the crash test. The workflow proposed in this paper is presented in Fig. 1. One practical aspect of this paper is a detailed description of the development of a numerical crash test model for a concrete barrier, along with a description of the validation process. Additionally, a detailed presentation of the internal force and moment envelopes during a crash is provided.

The above objectives are important since there are a limited number of articles demonstrating concrete barrier performance. Some of the available papers use linear material laws for concrete [17, 18, 35], which might be suitable for recreating the test course but do not give full insight into the damage mechanisms in the barrier. Others focus on different perspectives from which the concrete can be considered rigid [20, 25, 27]. The usage of more complex concrete material laws has also been discussed in earlier papers [12, 36]. This article, however, proposes the application of the Continuous Surface Cap Model (CSCM) for the modeling of the concrete material [37, 38]. This enables the reconstruction and analysis of the structural damage, including damage that emerges inside the structure. Furthermore, it allows a deeper analysis of the internal forces arising during a vehicle crash.

This paper is organized as follows. The first section describes the research methods and the numerical modeling details. The full-scale crash test setup is presented. Then, a detailed description of the numerical crash test model and its specific components is provided. The next section reports the results obtained in the validation and presents a detailed model analysis. The paper is concluded with a brief summary.

The paper uses keyword names in accordance with the LS-DYNA documentation [39, 40]. The names and abbreviations of the crash test indices are given in accordance with EN 1317 [5, 6]. For all material data, units of t, N, mm, and s are used, unless stated differently. As impact severity indices, the acceleration severity index (ASI) and the theoretical head impact velocity (THIV) were calculated in accordance with the European standard EN 1317 [5, 6]. The values were obtained using proprietary codes, whose results were compared with those obtained from the certification body.

2 Materials and methods

2.1 Description of the full-scale TB41 H2/W5/B concrete barrier crash test

The full-scale crash test was conducted on the 29th of June 2017 by the Road and Bridge Research Institute (IBDiM, www.ibdim.edu.pl) in the Research Institute for Protective
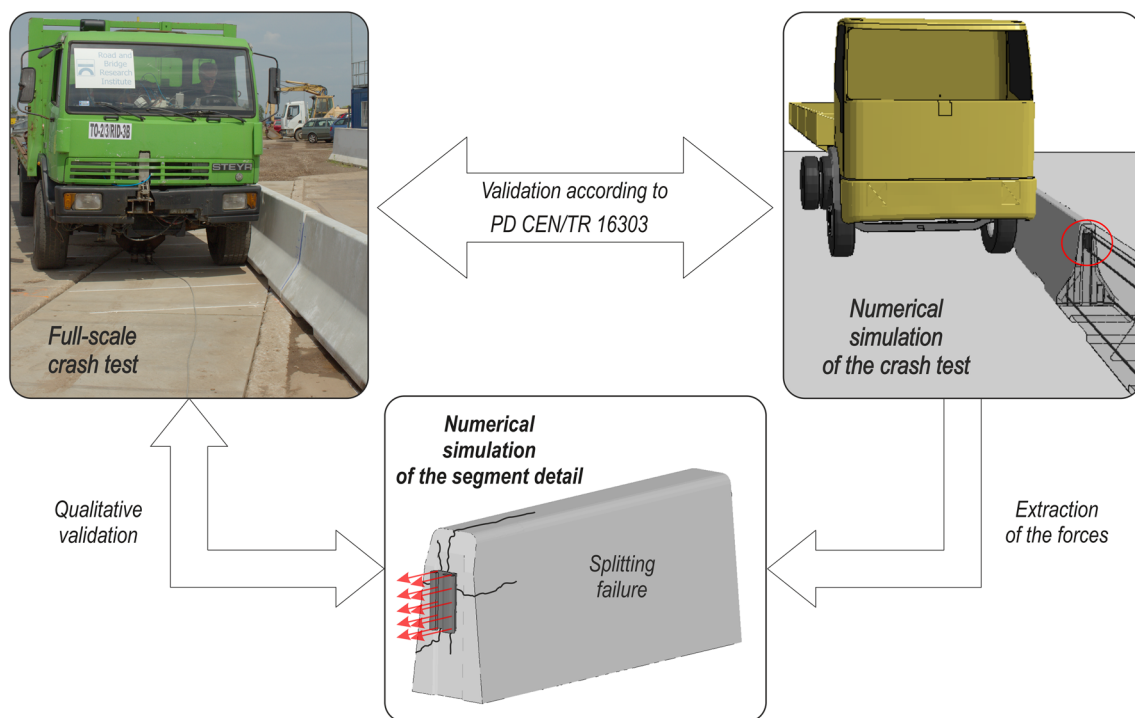

Fig. 1 Workflow of the experiments described in this paper

Systems (IBOS, www.ibos.com.pl) in Inowrocław, Poland. The test was carried out as part of the research project "The impact of time and operating conditions on the durability and functionality of traffic safety protection elements" (acronym *LifeRoSE*). The examined barrier, of class H2/W5/B [6], consisted of 6 segments made of reinforced concrete. Each single segment was 8 m long and 0.8 m in height, resulting in a total system length of 48 m. The scheme of the test setup, with the segment numbering that will be used in later parts of the paper, is depicted in Fig. 2. Figure 3a shows two of the segments composing the system. Adjacent barrier elements were connected using coupling elements, as seen in Fig. 3b. The barrier was placed mostly on a concrete surface; however, there was a short distance along which it crossed a gravel path, as shown in Fig. 3c. To perform the TB41 [6] crash test, the 10 t HGV - STEYR 12S18 was used.

2.2 Description of the numerical simulation of the crash test

Each segment of the barrier consisted of concrete, steel coupling elements, stirrups, and reinforcement bars. The geometry of the barrier was recreated in accordance with the design documentation and in situ measurements. First, the outer geometry of the concrete was recreated in detail (see Fig. 3a). Then, the coupling elements and reinforcements were embedded in each segment. Due to the

capabilities of the computational software and to achieve a balance between detail and robustness, the concrete solid was chosen to overlap with the coupling elements and reinforcements. In later steps, in the detailed model, these objects were modeled explicitly by cutting a segment out of the concrete solid.

FE discretization was performed in the ABAQUS software, and then, in some cases, LS-PREPOST was used to maintain appropriate mesh control. Two segments of the system (2e and 3e in Fig. 2), at the location of direct impact, were discretized using tetrahedral elements with an average characteristic size of 38 mm. The FEs of the concrete regions in the remaining barrier segments were also tetrahedral but with a coarser mesh, with a size of approximately 100 mm. The steel regions were meshed independently, with elements of approximately 10 mm for the couplings (solid FEs) and 50 mm for the reinforcement bars (beam FEs). A close-up view of the mesh may be seen in Fig. 4. The reinforcement bar was connected to the coupling element with one shared node and an overlapping beam element to preserve a stiff connection.

As mentioned before, no space was left in the concrete region for reinforcement. Thus, each steel part was coupled to the concrete using the *CONSTRAINED_LAGRANGE_IN_SOLID technique with the default settings, which coupled the displacements of the nodes of the steel FEs with the displacements of the surrounding concrete solid.
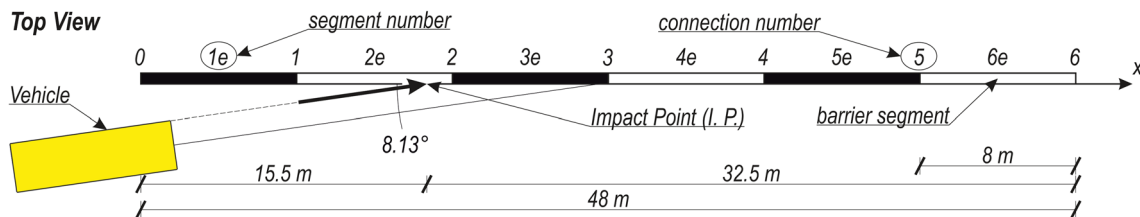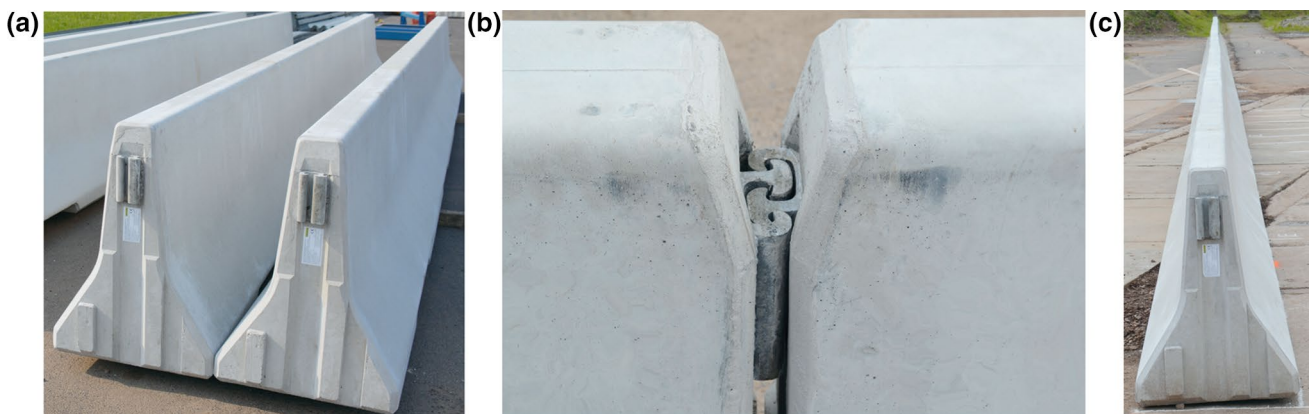

Fig. 2 Scheme of the test setup

Fig. 3 General view of the: **a** two segments, **b** a detailed connection with the coupling elements, and **c** the whole barrier on the ground
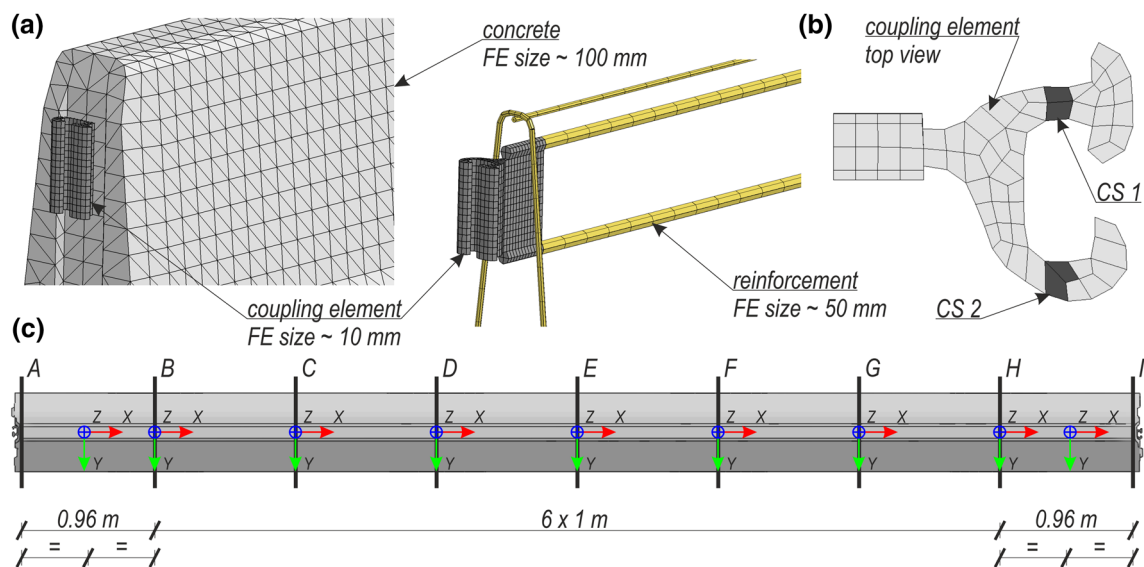
Fig. 4 Concrete segment description: **a** segment mesh details, **b** top view of a coupling element, and **c** cross-section locations

To obtain the resultant forces from the different cross sections of the barrier segments, the *DATABASE_CROSS_SECTION_PLANE and *DATABASE_CROSS_SECTION_SET keywords were used. The first one was used at every meter along the length of the segments. The latter was adopted to calculate the forces in the coupling elements because they consisted of uniformly distributed elements. It was necessary to follow up the creation of the cross sections with the definition of corresponding coordinate systems. This is because the segments move during a vehicle impact; hence, the coordinate systems need to move with the cross sections. The coordinate systems were attached to the bottom nodes of the system, which were less likely to erode during the simulation. Figure 4 depicts the described features. Figure 4a shows illustrations of the segment parts. Figure 4b presents a top view of a coupling element, with the element lines for the force calculations marked in dark gray. Figure 4c shows a barrier segment, with cross sections A–I marked with black lines. Each cross section is assigned to the corresponding (closest) coordinate system. For cross sections A and I, the corresponding coordinate system is 0.48 m away from the section.

All concrete parts of the system were modeled using the *MAT_CSCM [37, 38] material law. The constitutive relations were described by a continuous surface cap with a smooth intersection between the shear yield surface and hardening cap. The damage formulation was based on cumulative strain energy, with techniques to preserve the mesh size objectivity. Separate damage criteria were calculated depending on the stress state of the elements, namely ductile and brittle damage criteria. Strain rate effects were considered by means of viscoplasticity. The data

calibration process for this advanced constitutive relation is described in Ref. [41]. The authors provide the theoretical background and compare the results for two material laws that can be used to model the mechanical behavior of concrete. However, in this paper, *MAT_CSCM [37, 38] is used because of its robustness and reports that prove its reliability. Bielenberg et al. [42] published a report where the development of a temporary concrete barrier was described. The authors reviewed the existing designs from literature and conducted numerical simulations to find the most appropriate design for their application. The concrete barrier was modeled using *MAT_CSCM and proved to provide reliable results. Another report on the topic of vehicle crashes into the concrete structures was published in 2016 by Agrawal et al. [43]. It considered the trucks impacting the highway bridge piers. The authors firstly validated the concrete material model and then applied it to the numerical simulations of the impacts. Next, the two more research papers by Zhou et al. [44] and Miśkiewicz et al. [45] presented the application of the *MAT_CSCM concrete material model in the impact analysis. The first one considered the vehicle impacting the bridge pier and the second a truck with assembled hydraulic crane that hit the lower parts of the viaduct. Both applications provided results that are the source of valuable conclusions.

The concrete model needs the initial parameters to work properly. The most important initial material input was acquired from laboratory tests and is provided in Table 1. Another important feature of this material law is its mesh objectivity [37, 38], which appears to be crucial when using a strongly nonuniform tetrahedral mesh. The

Table 1 Description of the model details

Item	Description
VRS concrete	Mesh: 4-node solid TET4 FEs; 1 integration point (LS-DYNA element type 10 [39, 40]);
	19,871 FEs in segments 1e, 4e, 5e, and 6e; 207,918 FEs in segments 2e and 3e,
	*MAT_CSCM [37, 38],
	Material parameters: $F_c = 48.2$ MPa, Dagg $= 34$ mm,
	$\rho = 2.32e^{-9}$t/mm^3, Irate $= 1$, Erode $= 1.1$, Recov $= 1$,
	where F_c is the unconfined compression strength, *Dagg* is the maximum aggregate size, ρ is the mass density, *Irate* determines whether strain rate effects are considered, *Erode* specifies the maximum principal strain value (Erode–1.0) for element erosion, and *Recov* describes the modulus recovery based on the sign of the pressure invariant, where 1 indicates full recovery
VRS steel: Coupling elements Reinforcement	Mesh: 8-node solid HEX8 FEs; 1 integration point (LS-DYNA element type 1 [39, 40]);
	2348 FEs per segment,
	Mesh: 2-node beam tubular FEs; Hughes-Liu cross-section integration;
	2x2 Gauss quadrature (LS-DYNA element type 1 [39, 40]); 1041 FEs per segment,
	*MAT_PIECEWISE_LINEAR_PLASTICITY [39, 40],
	Material parameters: $\rho = 7.8e^{-9}$t/mm^3, $C = 40.4s^{-1}$, $P = 5$, FAIL $= 0.5$,
	where ρ is the mass density, C and P are the parameters for the Cowper-Symonds rate term, and FAIL is the effective plastic strain value for element deletion
Road surface	*MAT_RIGID [39, 40],
	Mesh: 4-node shell QUAD4 FEs; Belytschko-Tsay reduced integration (RI)
	(LS-DYNA element type 2 [39, 40]); 1800 FEs
Summary	Mesh: 508,408 solid FEs, 6246 beam FEs, 1800 shell FEs

tetrahedral FE formulation uses constant stress elements with 1 integration point.

The constitutive law for the steel elements was described using a piecewise linear plasticity model with isotropic hardening and strain rate effects. The strain–stress curves were adopted from laboratory static tensile tests. Since no severe plastic strains in the steel were anticipated, the element deletion condition was set to FAIL $= 0.5$ (see Table 1). The Cowper-Symonds [46] strain-rate parameters were set equal to those used widely in the literature, e.g., by Wu et al. [47], and are provided in Table 1. The beam elements were formulated using the 2×2 Gauss quadrature Hughes–Liu cross-section integration formula, and the steel solids were described with 1-point integration for the hexahedrals.

Since no erosion of the road surface was considered, the *MAT_RIGID material model was used to model its behavior. The whole barrier model consisted of 516,454 FEs, and a brief summary is provided in Table 1.

The numerical model of the vehicle used in this paper was originally developed in 2005 by a research team from Politecnico di Milano studying impact analysis: Marco Anghileri, Luigi Castelletti, and Maro Mongiardini. This vehicle model was used, e.g., in papers [48, 49], and its 38 t version was also used in the article [50]. Although some parts of the model remained unchanged, the numerical vehicle model was subjected to some minor modifications before a successful application. e.g., tires are in direct contact with the VRS, hence proper modeling should be applied. In 2007 Reid et al. [51] developed a detailed tire model for the vehicle crash applications. This model takes into account all of

the tires major components and still preserves the low number of FEs to ensure low computational cost. Baranowski et al. [52] proposed a much more detailed approach, ensuring the maximum accuracy by multistage validation. Lastly, Gutowski et al. [53] showed the description of the modifications applied to the tires in the 1996 Dodge Neon numerical model. The aforementioned modifications to the tire were enough to provide reliable results for vehicle impacting the barrier behind the curb. This is a similar case to the vehicle driving over the foot of the concrete barrier's segment. Now, a brief description of the model after applying these modifications is provided as follows.

First, some basic remeshing was performed to eliminate initial penetrations and to increase the accuracy on the side of direct impact. Afterward, the model consisted of 40,212 shell elements, 1091 solids, and 68 beams, comprising 36,799 nodes. The shells were formulated using the Belytschko–Tsay full integration (FI) scheme with five integration points through the thickness. For some of the parts, Hughes–Liu elements with reduced integration (RI) were used instead. The solid parts that shared nodes with shells were described by FI solids with additional nodal rotations; for the rest, RI solids were used. Regarding the beams, Hughes-Liu beams with cross-section integration were used. Most material models consider elasticity and piecewise linear plasticity [39, 40]. The tires of the vehicle were modeled using the control volume approach and were inflated with air to a pressure of 0.5 MPa using the *AIRBAG_SIMPLE_AIRBAG_MODEL keyword. The mechanical behavior of the outer layers of the tires was

described with the *MOONEY_RIVLIN_RUBBER material model. An additional elastic 0.2 mm steel plate coinciding with the rubber parts was used to represent the tire reinforcement. This tire modeling technique was adopted from the coach model developed by the Norwegian Public Road Administration (www.vegvesen.no) and based on the suggestions found in the papers described earlier [51–53]. Another change, applied to the HGV model, was the simplification of material description of the fuel in the tank. The mechanical model was changed to elastic since it showed unstable behavior in some cases and was not relevant to this application. One of the major improvements was the usage of eight beams instead of a rigid connection between the vehicle and the front axle. This modification was made to capture the collapse of the suspension. The initial velocities of the vehicle's nodes were introduced using the *INITIAL_VELOCITY_GENERATION keyword. The nodes were divided into two sets: wheel nodes, with translational and rotational velocity, and the remaining nodes, with solely translational velocity.

A general view showing a comparison of the actual vehicle and the vehicle model is depicted in Fig. 5. During the full-scale crash test, the HGV had an accelerometer mounted on the front dashboard; thus, a similar one was introduced in the model. A detailed description of the model's geometry, with the location of the accelerometer, is shown in Fig. 6. The corresponding vehicle dimensions are presented in round brackets. A brief summary is presented in Table 2 to compare the numerical model with the full-scale vehicle and the EN 1317 [6] requirements.

The simulation contained several contact definitions, comprising several contact pairs. Two types of contacts implemented in LS-DYNA [39, 40] were used: an automatic single-surface contact and an automatic surface-to-surface contact. For all used contacts, the forces were calculated based on the nodal masses and time steps to properly model the contact interface forces between parts with dissimilar material properties. First was the automatic single-surface contact SOFT = 1 for the vehicle, excluding its tires and

the VRS, with the following specified friction coefficients: $f_s = 0.3$ and $f_d = 0.2$, where f_s is the static friction coefficient and f_d is the dynamic friction coefficient. Then, there was the automatic surface-to-surface contact SOFT = 2 for the vehicle's tires with the VRS and the rigid shell representing the ground, with friction coefficients of $f_s = 0.9$ and $f_d = 0.8$. Finally, another automatic surface-to-surface contact SOFT = 1 was introduced to account for the friction between the VRS and the ground, with coefficients of $f_s = 0.45$ and $f_d = 0.315$. Each contact had a decay coefficient equal to $d_c = 10^{-3}$. The coefficients of friction were set on the basis of previous literature [39, 42, 54, 55] and several preliminary parametric studies. Mass damping was used with a constant Rayleigh damping coefficient of $\alpha = 0.01$. Since mostly FI shell elements were used in the simulation, an hourglass formulation IHQ = 8 was used, with an hourglass coefficient of QH = 0.03. This activates the full warping stiffness for FI shell formulations (a 25% speed penalty is common for this option). Another important feature, used to reduce the calculation time, was the mass scaling technique, with the initial time step set to 10^{-6}s. This resulted in an artificial addition of 58 kg, which corresponds to 0.15% of the total system mass. All of the aforementioned remaining model parameters are listed in Table 3.

2.3 Description of the numerical model of the isolated concrete segment

Another numerical model that was analyzed was a segment cut from the original barrier segment no. 2 (see Fig. 2). The cut dimensions were 1 m in length and 0.4 m in height, as shown in Fig. 7a. Tetrahedral elements with 1-point integration were used to model the concrete part of the segment. This part was tailored to leave an empty space for the main reinforcement and the coupling element; see Fig. 7b. A variable-size mesh was used: In the region adjacent to the coupling element, the element size was approximately 4–5 mm, and with increasing distance from this region, the size of the elements nonlinearly increased to a maximum
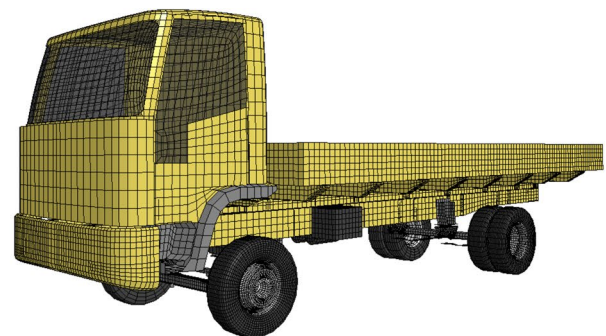

Fig. 5 Comparison between the actual vehicle and its numerical model
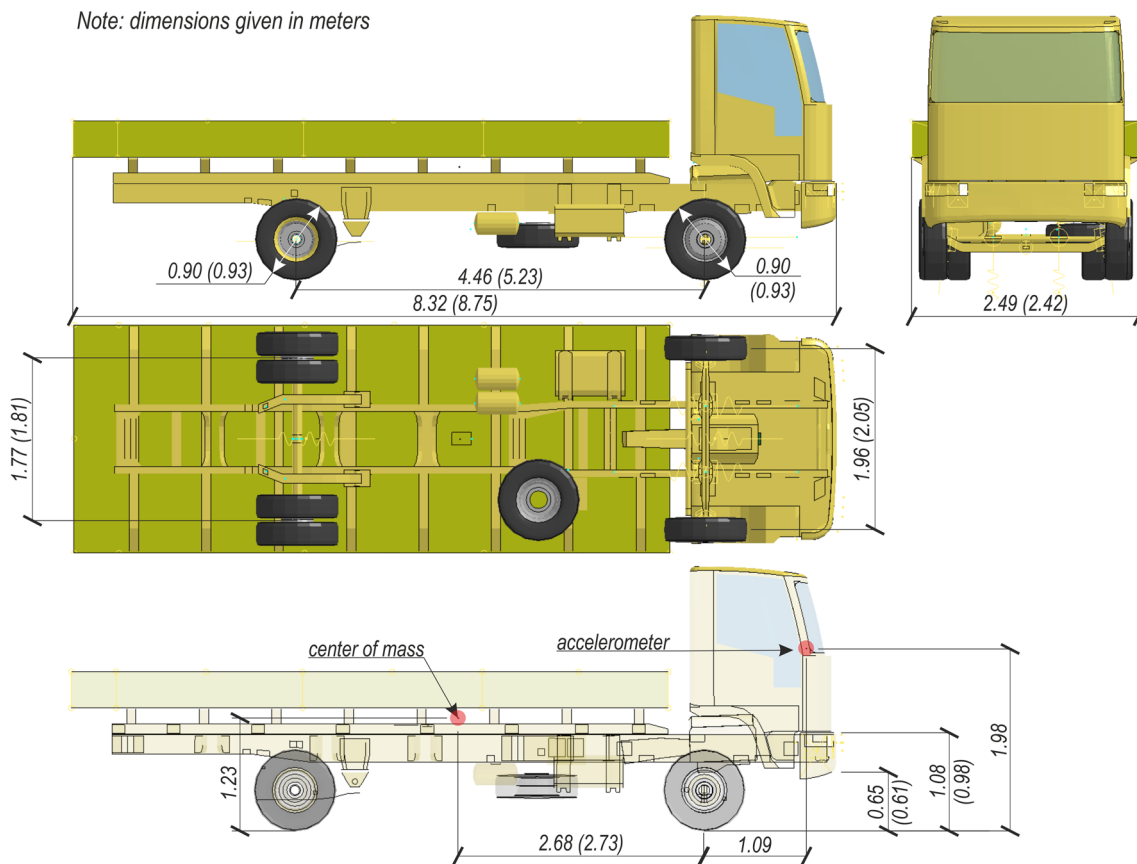
Note: dimensions given in meters

Fig. 6 Description of the detailed model geometry and the accelerometer location (corresponding full-scale vehicle dimensions shown in round brackets)

Table 2 Comparison of the numerical model, the full-scale vehicle and the EN 1317 requirements

|	Numerical model	Vehicle	EN 1317 requirements	Condition
Name	Rigid HGV 10t	n/a	n/a	
Number of axles	1 steering + 1	n/a	n/a	
Mass (kg)	10,068.3	9776.6 ± 16	10000 ± 300	Fulfilled
Length (m)	8.32	8.75 ± 0.02	n/a	n/a
Width (m)	2.49	2.42 ± 0.01	n/a	n/a
Center of mass location (mm)	CGX : 2690 CGY : 1 CGZ : 1239	CGX : 2730 ± 2 CGY : 4 ± 2 CGZ : 1516 ± 2	CGX : 2700 ± 270 CGY : ±100 CGZ : 1500(+225, −75)	Fulfilled Fulfilled Not fulfilled
Wheel track (front and rear) (m)	1.98 1.77	1.81 ± 0.01 2.05 ± 0.01	2.00 ± 0.30	Fulfilled
Wheel radius (unloaded) (m)	0.45	0.49 ± 0.01	0.46 ± 0.07	Fulfilled
Wheelbase (between extreme axles) (m)	4.45	5.26 ± 0.02	4.60 ± 0.69	Fulfilled
FEM details	36,799 nodes 41,401 FEs	n/a	n/a	n/a

n/a not applicable

value of approximately 30 mm. The mesh details are depicted in Fig. 7c. The solely concrete part was discretized into 155,713 nodes and 851,622 FEs. For the coupling and main reinforcement, an RI solid element formulation was also used; however, hexahedral elements were used for these regions due to their regular shape. Since no severe

Table 3 Remaining model parameters

Item	Description	
Contact	Vehicle w/o tires versus VRS	$f_s = 0.30; f_d = 0.200; d_c = 1e^{-3}$
	Vehicle's tires versus VRS and ground	$f_s = 0.90; f_d = 0.800; d_c = 1e^{-3}$
	VRS versus ground	$f_s = 0.45; f_d = 0.315; d_c = 1e^{-3}$
Damping	Constant mass damping	$\alpha = 0.01$
Hourglass	IHQ = 8	$QH = 0.03$
Time step control	Mass scaling at first step to time step (added mass = 58 kg, percentage increase = 0.15%)	$dt2ms = 1e^{-6}$s
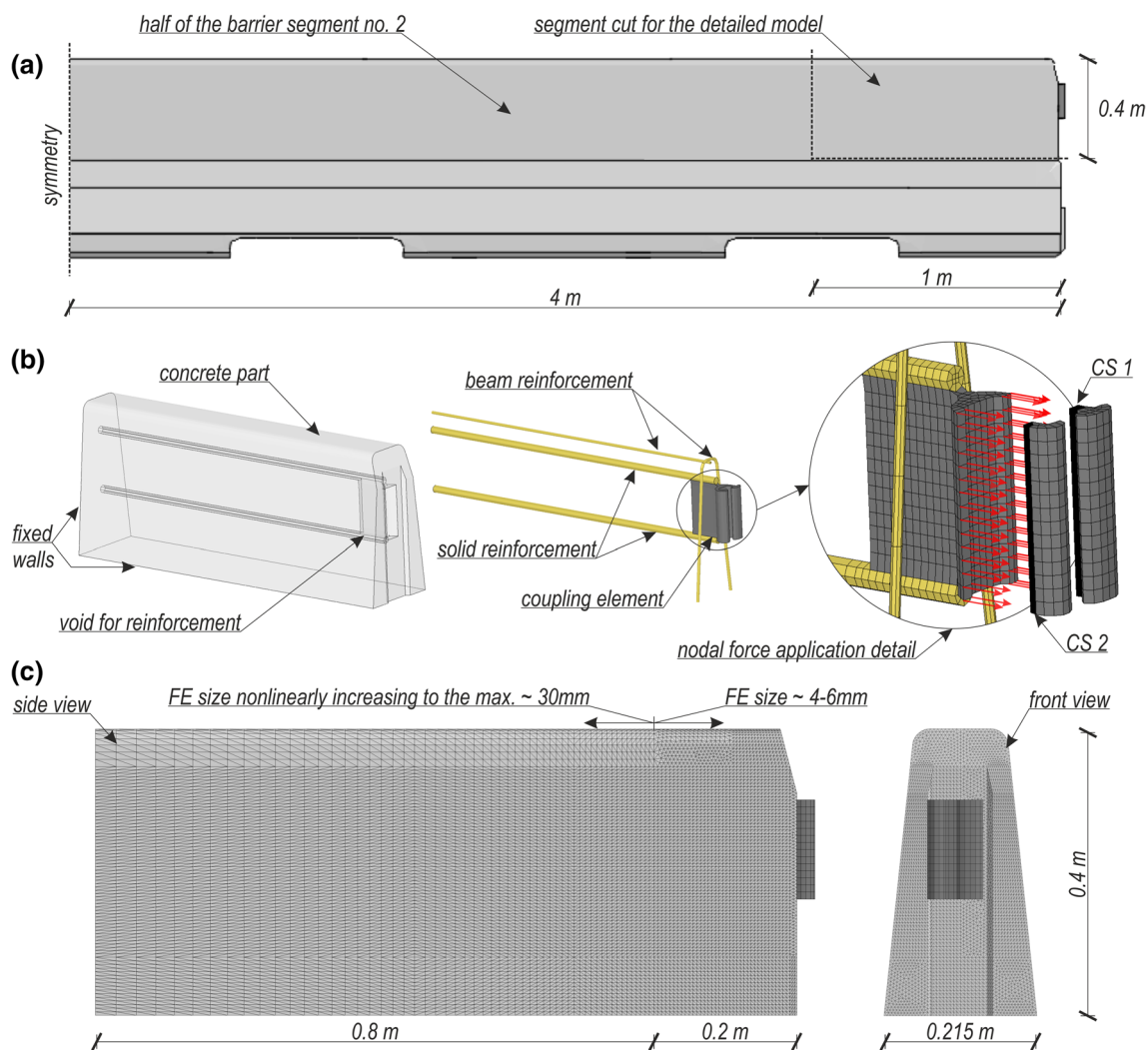
Fig. 7 Isolated segment cut from segment no. 2: **a** dimensions, **b** component details, and **c** mesh data

deformations were expected in the steel parts, the mesh size used near the region of applied force was equal to 5-10 mm. Then, 50 mm elements were used in the reinforcement, corresponding to the length of the beam elements in the full-scale analysis. The remaining steel reinforcement bars, with a diameter of 8 mm, were modeled using the same specifications as in the initial model described in Sect. 2.2.

The material models in this detailed segment were left unchanged relative to the initial model. However, a different approach was used for the coupling between the steel and the concrete. Instead of using a constrained formulation, the coupling was modeled using a penalty-based contact formulation with friction coefficients of $f_s = 1.0$, $f_d = 0.7$, and $d_c = 10^{-3}$. An additional viscous damping equal to 20% of

the critical damping coefficient was used to avoid parallel oscillations of the surfaces in contact. Since materials of dissimilar properties were intended to be in contact, the SOFT = 1 option was used to calculate the contact force [39, 40]. Finally, an additional layer of null shells, with a thickness of 0.01 mm, was applied to the surfaces of the parts in contact to apply the initial force perpendicular to the outer surfaces of the reinforcement and maintain the proper transmission of the friction forces.

All nodes on the outer surfaces that were formed as a result of cutting the detailed segment out of the entire barrier segment were fixed, as seen in Fig. 7b. The Rayleigh mass damping coefficient was constant and equal to $\alpha = 0.01$. The forces obtained from cross sections CS 1 and CS 2 (see Fig. 4b) during the full-scale crash test simulation were then applied through the nodes of the coupling element in the detailed model, as shown in Fig. 7b.

3 Results and discussion

3.1 Full-scale crash test validation

During the full-scale TB41 crash test, the 10 t vehicle struck the barrier at a distance of 50 cm from connection no. 2 (Fig. 2). The measured impact speed was 73.5 km/h, and the angle was 8.13°; thus, the deviation requirements according to the EN 1317 standard [6] were met. At the moment of impact, the front left wheel drove over a barrier segment, resulting in tire blow-out. This event was followed by an elevation of the front of the vehicle caused by the shape of the barrier. Then, the truck began to be redirected and fell back to the ground. After the suspension hit the ground, breakage of the left part of the suspension was observed as the vehicle started to lean and push against the barrier. Eventually, the rear of the vehicle hit the barrier approximately 250 cm behind connection no. 2. Then, the vehicle was properly redirected and continued its movement nearly parallel to the barrier face. The full-scale crash test resulted in a normalized working width of 0.9 m, and the barrier was classified as class W3 [6]. The corresponding dynamic

deflection was 0.4 m. The vehicle remained in contact with the barrier for approximately 12.15 m. The static working width of the barrier was measured to be 0.89 m. In this test, the ASI reached a value of 0.52 at a time of 0.225 s, which was the moment after full deflation of the front left tire. The THIV was 10 km/h. These index values correspond to the impact severity of level A in the test. It should be clarified that, according to the EN 1317 standard [6], this impact severity level determination is designed for cars; however, such tests are not a subject of analysis in this paper. It is known that the ASI and THIV values are higher in tests of passenger cars than in tests of trucks and buses. Moreover, characteristic cracks were found in some segments of the barrier (no. 2-5), as shown in Fig. 8. Segments no. 1 and no. 6 did not show clear signs of damage.

In the corresponding numerical simulation of the TB41 crash test, the 10 t HGV hit the system at the same impact point as on the test site. The speed and impact angle were also set to match the conditions from the experiment. The vehicle model drove onto the barrier segment, and the wheels were turned to the left. The maximum value of the front left tire's pressure obtained during the simulation was equal to 0.57 MPa, which corresponds to an increase of approximately 14.9% relative to the initial pressure. In the current model, tire blow-out and suspension breakage were not considered. Thus, after driving onto the segment, both front wheels lost contact with the ground. Then, the vehicle fell to the ground and started to be redirected. The rear of the vehicle hit the barrier approximately 150 cm behind connection 2 (Fig. 2). Since neither the left front wheel nor the suspension was damaged, the vehicle did not lose its balance. However, the wheels were rotated to the left, as in the full-scale test. Therefore, the truck was stuck against the barrier and was constantly trying to drive onto the next segment. Finally, behind connection no. 4, the truck was pushed away from the barrier. The HGV continued to hit the VRS and be pushed back until the end of the simulation. The numerical test resulted in a normalized working width of 0.9 m, classifying the tested barrier as class W3 [6]. The obtained dynamic deflection was 0.4 m. The contact length between the vehicle and the barrier was 18.3 m.
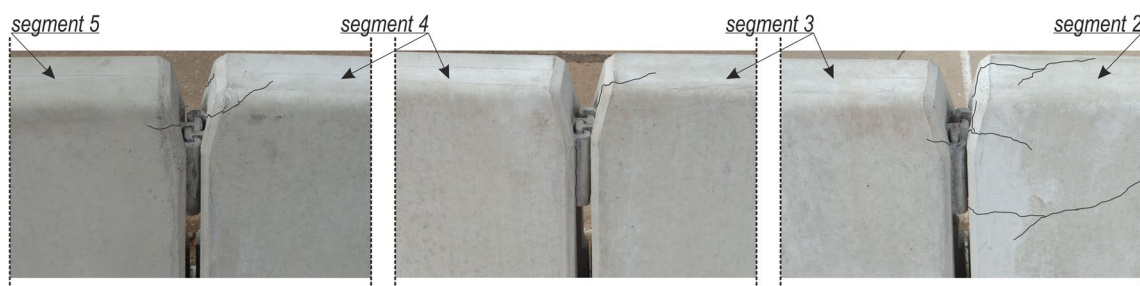

Fig. 8 Views of some of the cracks observed in the VRS segments

Thereafter, the contact was terminated, although due to the rotation of the wheels, contact was restored after 0.1 s. The maximum permanent deflection was measured to be 0.94 m. The impact severity assessment indices were as follows: ASI = 0.51 at time 0.119 s and THIV = 13 km/h.

A visual representation of the vehicle trajectories in both the full-scale crash test and the numerical simulation is presented in Fig. 9. The comparison starts at the time of impact and is presented in time intervals of 0.1 s. A general comparison of the barrier deformation after the crash is depicted in Fig. 10. The ASI and Theoretical Head Velocity (THV) curves were compared using the RSVVP software [56, 57], which can calculate MPC and ANOVA comparison metrics. The THV curve represents the speed of the theoretical head up to the moment of impact of a theoretical vehicle cabin with the dimensions given in the EN1317 standard. The ASI function is presented in Fig. 11. Most of the metrics pass the conditions established in a previous technical report [31]. However, inter alia, due to the lack of tire blow-out and suspension breakage in the virtual test, the ANOVA average ASI metric fails by 1.1%. The relation between the THV curves from the real test and the simulation is presented in Fig. 12. The metrics show good correlation since all validation conditions were met. A graph presenting the lateral displacement of the concrete barrier measured after the test is shown in Fig. 13. The impact point is marked by an arrow pointing in the initial velocity direction and labeled I.P. The maximum discrepancy is found to be near the impact point, precisely at connection no. 2. It amounts to 7.7 cm and is lower than the uncertainty of the real test's measurements (± 10 cm). The average value of the displacement differences is 1.5 cm. The validation is concluded in Tables 4 and 5. These tables contain specific validation requirements, the majority of which are fulfilled. Additional verification and evaluation criteria proposed in the European guidelines for computational mechanics [30–32] and adapted, e.g., in papers [58, 59] were also checked. Only the criterion concerning the time at which the maximum ASI value occurred was not satisfied. In the virtual test, the maximum ASI was reached 0.106 s later, while the criterion allows a 0.05 s difference. However, in justified cases, the technical report [32] allows a simulation to be validated without satisfying all requirements. In the authors' opinion, the presented case can be justified because the general trend of the measures is maintained. Moreover, the standard [60] does not require measuring the impact severity indices for HGVs; however, for the purpose of this analysis, it was decided to check these indices to enhance the reliability of the simulation.

Since the simulation results are considered validated, further analysis of the results can be performed. First, the cross-sectional forces for all 54 segment cross sections will be presented. For convenience, the cross-section locations for each segment (Fig. 4) are presented again in Fig. 14a.

The X direction of the cross sections coincides with the direction of movement. Envelopes of the three forces were created from the simulation data as a whole. The representation described above is depicted in Fig. 14b–d. All of the force plots include the VRS on their right-hand sides. The impact point is labeled I.P. The *ForceX* envelope shows the dominance of the longitudinal compression forces. The maximum compression force in the simulation amounts to $F_{X,c} = 315.52$ kN. This force acts in cross section 4I, close to connection no. 4 (Fig. 2). The peak of the tension force is 65.5% smaller, equal to $F_{X,t} = 108.94$ kN (cross section 5B). It was found that tension was transferred through the reinforcement bars, while the concrete bore the compression. The large compression forces on the envelope were due to the shock wave that was initiated by the truck's impact and traveled through the barrier. This phenomenon is depicted in Fig. 15. The graph in Fig. 14c represents the *ForceY* envelope, also called the transverse force. The values observed in this force component are noticeably smaller. The minimum value is 78.2% lower than its longitudinal counterpart and amounts to $F_{Y,\min} = -68.77$ kN (cross section 2I). The maximum value of *ForceY* is equal to $F_{Y,\min} = 60.80$ kN (cross section 2H). The last plot, Fig. 14d, shows *ForceZ*, which is regarded as the vertical force in the section. This component shows the least contribution to the resultant force, with $F_{Z,\min} = -52.61$ kN (cross section 3A) and $F_{Z,\max} = 58.09$ kN (cross section 2I). However, the vertical force envelope illustrates the characteristic behavior of the system, in which, after impact, adjacent segments are leaned against each other at the point of connection. For example, the rear side (cross section I) of each segment tends to have a force Z component that is directed downwards, unlike the front side (cross section A), where the force points in the opposite direction. This behavior is also visible on the right-hand side of Fig. 8, where the 'right' segments are slightly above the 'left' ones at each connection.

The next results, discussed below, consider the moment envelopes. The values were acquired from the same simulation, using the same cross sections as in the previous analysis. The descriptions are also the same. The resulting moment envelopes are depicted in Fig. 16. All moments were transformed to the center of the area of the corresponding cross section. First, from the left-hand side, is the Moment X envelope, which shows the least significant contribution. The minimum value is $M_{X,\min} = -31.49$ kNm, while the maximum is $M_{X,\max} = 17.13$ kNm. These values are found in the vicinity of the impact point. The middle envelope shows the moments around each segment's Y-axis. It can be observed that positive moments dominate the results. The peak value is reached near the location of impact (cross section 2H) and is equal to $M_{Y,\max} = 149.99$ kNm. However, similar values can also be observed in cross section 2G, with a value of $M_{Y,2G} = 132.93$ kNm, and cross
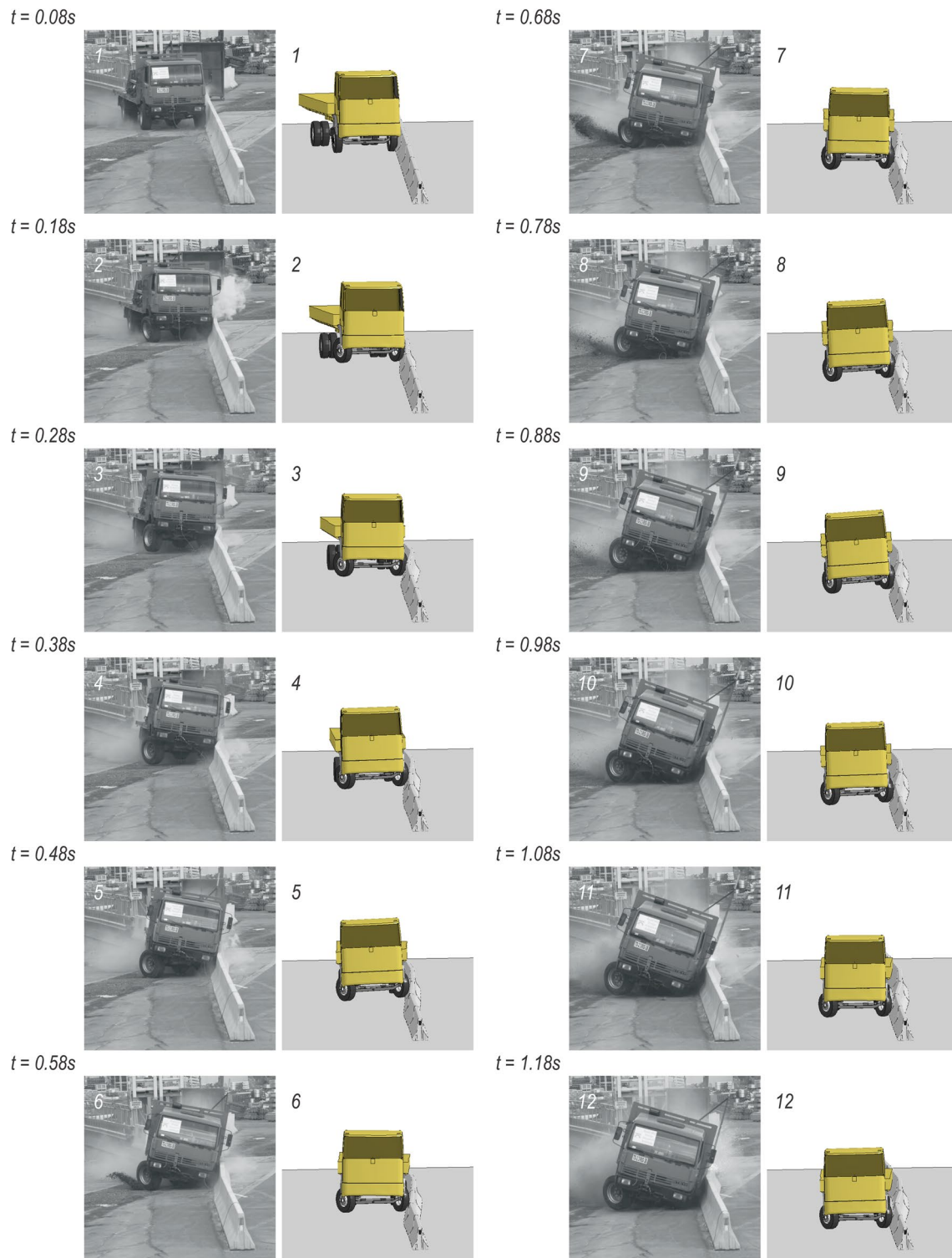
t = 0.08s

t = 0.18s

t = 0.28s

t = 0.38s

t = 0.48s

t = 0.58s

t = 0.68s

t = 0.78s

t = 0.88s

t = 0.98s

t = 1.08s

t = 1.18s

Fig. 9 Comparison of the trajectories in the full-scale crash test and the numerical simulation
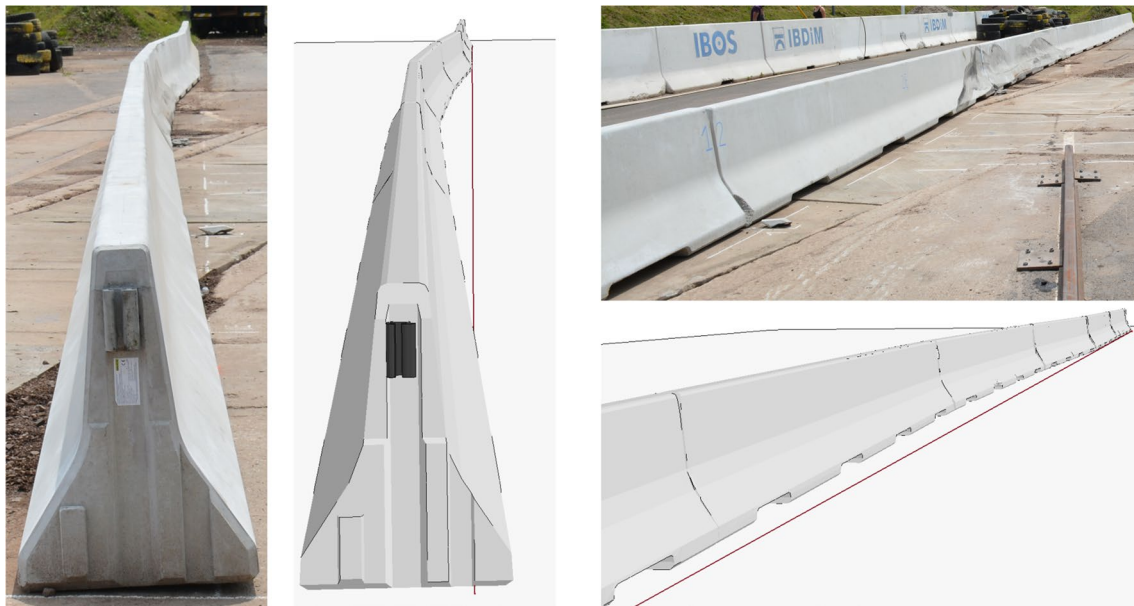
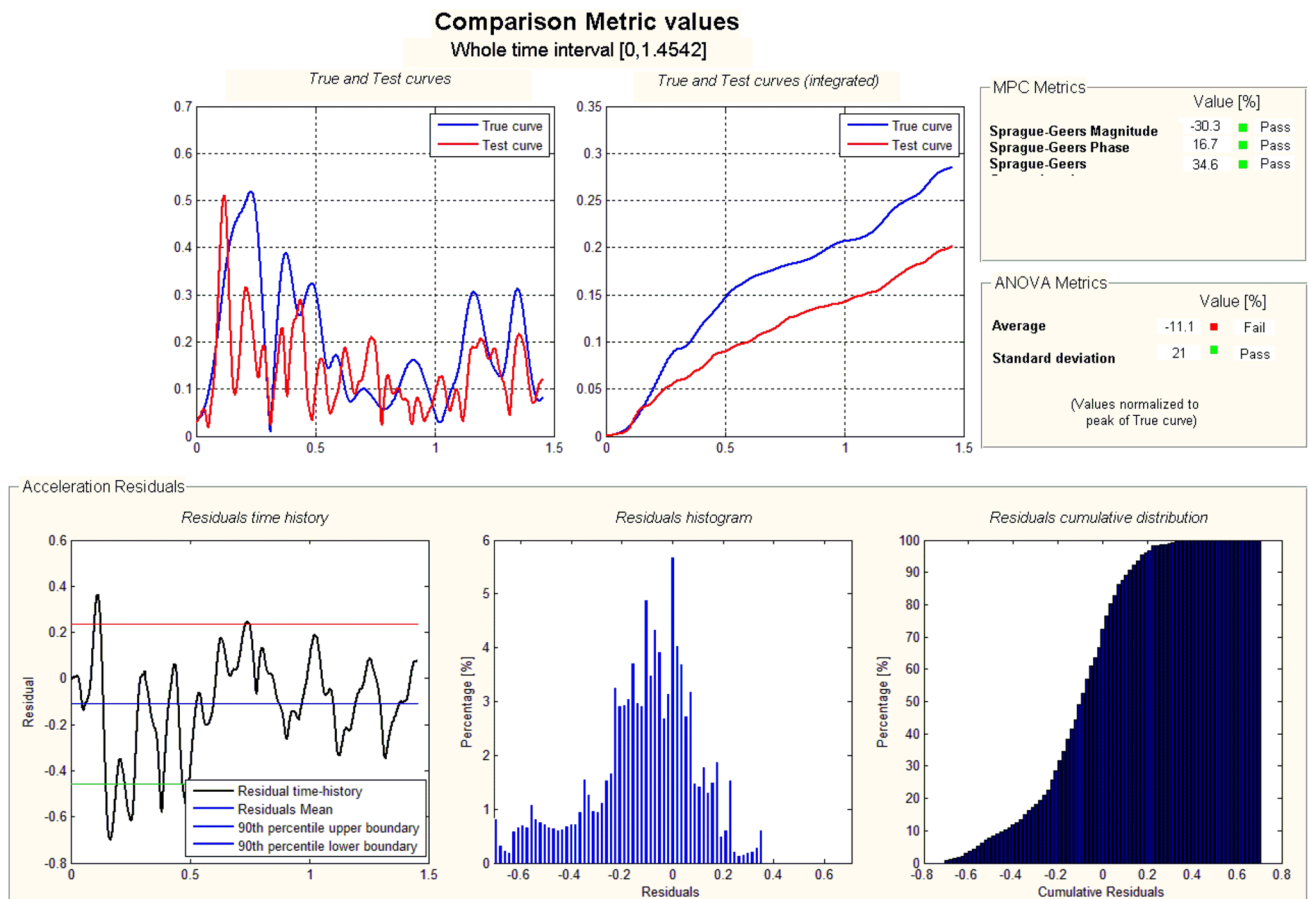**Fig. 10** Final deformations of the full-scale system and the numerical model after the test

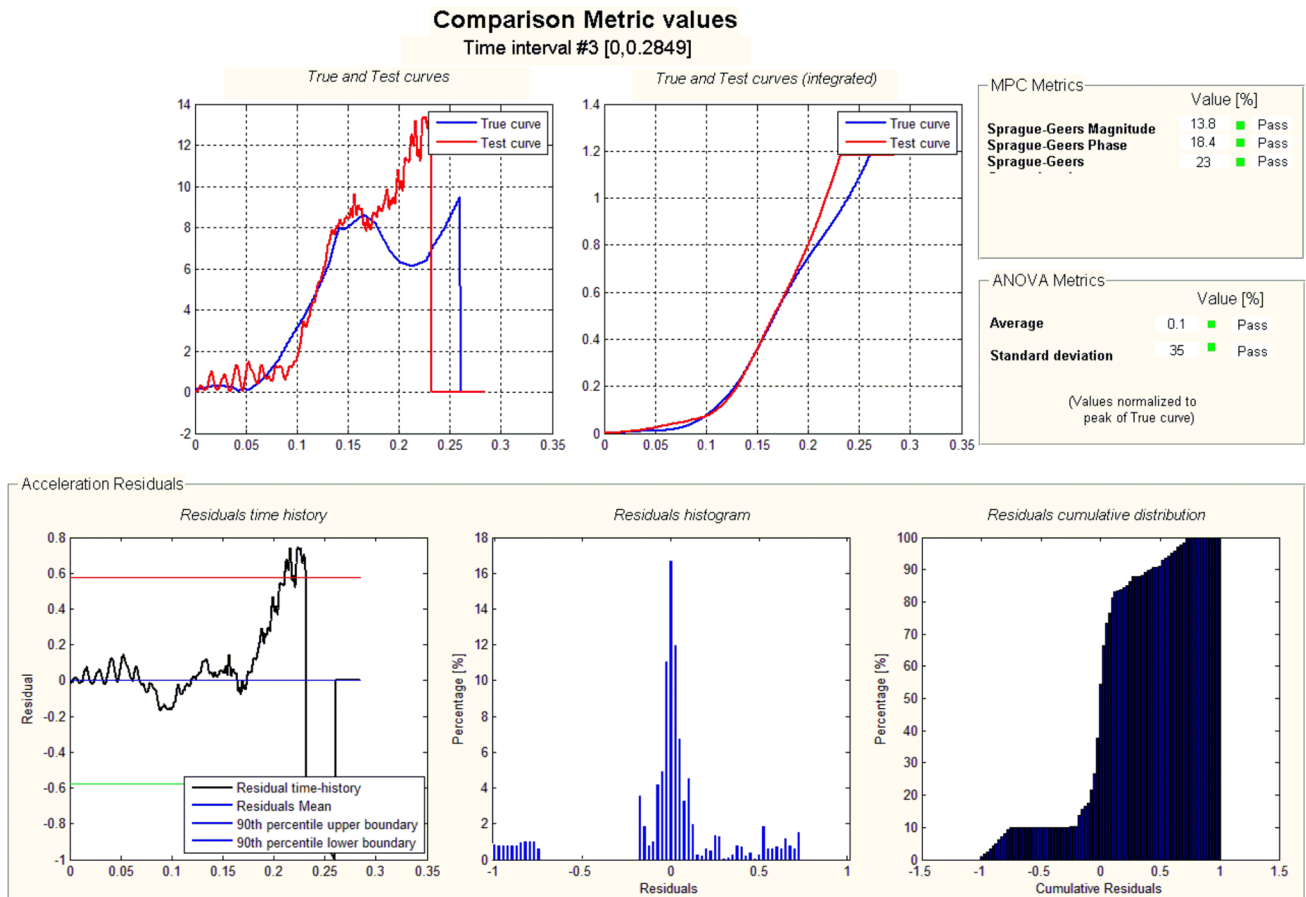**Fig. 11** Comparison of ASI curves using RSVVP code: blue—full-scale crash test; red—simulation

Comparison Metric values
Time interval #3 [0,0.2849]

True and Test curves

True and Test curves (integrated)

MPC Metrics

	Value [%]	
Sprague-Geers Magnitude	13.8	Pass
Sprague-Geers Phase	18.4	Pass
Sprague-Geers	23	Pass

ANOVA Metrics

	Value [%]	
Average	0.1	Pass
Standard deviation	35	Pass

(Values normalized to peak of True curve)

Acceleration Residuals

Residuals time history

Residuals histogram

Residuals cumulative distribution

Fig. 12 Comparison of THV curves using RSVVP code: blue—full-scale crash test; red—simulation
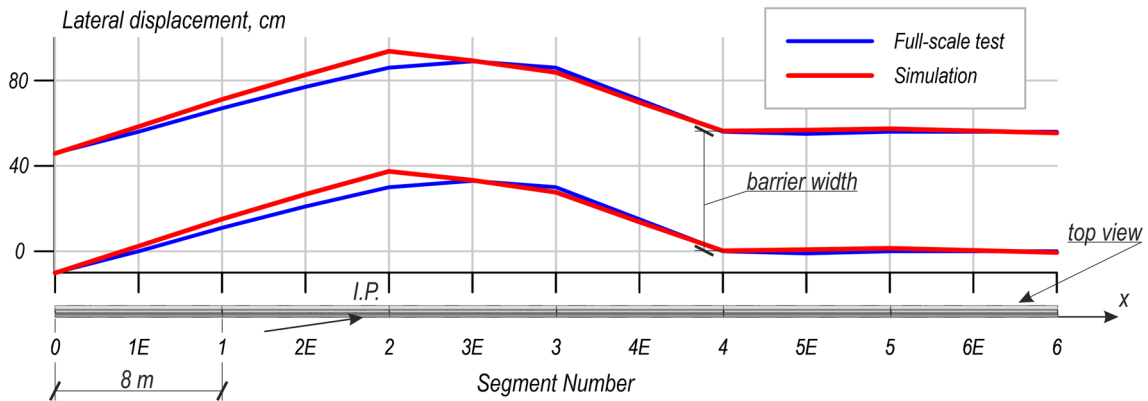
Fig. 13 Lateral displacement comparison

section 4I, where $M_{Y,4I} = 132.62$ kNm. The corresponding absolute value of the negative moment is 41.9% lower and is equal to $M_{Y,\min} = -87.20$ kNm. The final moment envelope reflects the pair of forces around the Z-axis. The maximum and minimum values in this case are of the same order of magnitude, being $M_{Z,\min} = -108.46$ kNm and $M_{Z,\max} = 109.56$ kNm. The following interesting result can be observed: the moments about the Y axis of the cross

Table 4 Assessment of the barrier deformation

Indicator	Numerical simulation	Full-scale crash test
Working width W_m (m)	0.94	0.97 ± 0.1
Normalized working width W_n (m)	0.9	0.9 ± 0.1
Class of normalized working width	W3	W3
Working width criterion (m) [30]	$0.97 - 0.94 \leq (0.05 + 0.1 \cdot 0.97)$ $0.03 \leq 0.147 \Rightarrow$ Fulfilled	
Dynamic deflection D_m (m)	0.38	0.4 ± 0.1
Normalized dynamic deflection D_n (m)	0.4	0.4 ± 0.1
Dynamic deflection criterion (m) [30]	$0.40 - 0.38 \leq (0.05 + 0.1 \cdot 0.40)$ $0.02 \leq 0.09 \Rightarrow$ Fulfilled	
Maximum permanent deflection (m)	0.94	0.89 ± 0.2
Length of contact (m)	18.3	12.15 ± 0.2

Table 5 Assessment of the impact severity

Indicator	Numerical simulation	Full-scale crash test
ASI (–)	0.5	0.5
ASI criterion (–)[30]	$0.54 - 0.52 \leq \pm 0.1$ $0.02 \leq 0.1 \Rightarrow$ Fulfilled	
Time ASI (s)	0.119	0.225
Time ASI criterion (s) [30]	$0.225 - 0.119 \leq \pm 0.05$ $0.106 \geq 0.05 \Rightarrow$ Not fulfilled*	
THIV (km/h)	13	10
THIV criterion (km/h) [30]	$13 - 10 \leq \pm 3$ $3 \leq 3 \Rightarrow$ Fulfilled	
Time of flight of the theoretical head (s)	0.23	0.28
Time of flight criterion (s) [30]	$0.28 - 0.23 \leq \pm 0.05$ $0.05 \leq 0.05 \Rightarrow$ Fulfilled	
Impact severity level	A	A

* The standard [30] allows, in justified cases, acceptance of a simulation that does not satisfy all requirements

sections are higher in magnitude than the moments about the Z-axis. This suggests that the reinforcement and concrete in the Y–Z plane are required to bear most of the forces and moments.

Following the creation of the above envelopes for all three forces and moments along the barrier, the forces occurring in the coupling between segments 2e and 3e will now be analyzed in detail. These values will enable the examination of the isolated concrete barrier segment in the next step of the analysis (Sect. 3.2). The corresponding curves are presented in Figs. 17 and 18. The forces on the time curves were extracted from the cross sections presented in the figures (denoted by symbols CS 1 and CS 2). Both figures present plots of the three force components, which are shown in different colors, as indicated in the legend. It is worth mentioning that the time scale does not correspond to the one used in the ASI calculation; hence, the following results cannot

be directly compared. In Fig. 17, the compression force (in the $-X$ direction) appears to be predominant. Its peak value is equal to $F_{X,CS1,min} = -351.86$ kN, while the remaining components have magnitudes that are lower by more than 90%: $F_{Y,CS1,min} = 33.50$ kN and $F_{Z,CS1,min} = -17.30$ kN. The next graph, presented in Fig. 18, shows the force versus time plots for cross section CS 2 of the coupling. As can be observed, the force components in this section have values lower than 1 kN, much less than those obtained in cross section CS 1. The presented force curves (Figs. 17, 18) were applied in the isolated segment simulation, discussed in the next section, to enable a thorough analysis of the cracking and damage resulting from the 10 t truck impact. Since the intent was to investigate splitting failure phenomena, only the presented longitudinal forces were applied. The truck's transverse force on the barrier segment was thus omitted.
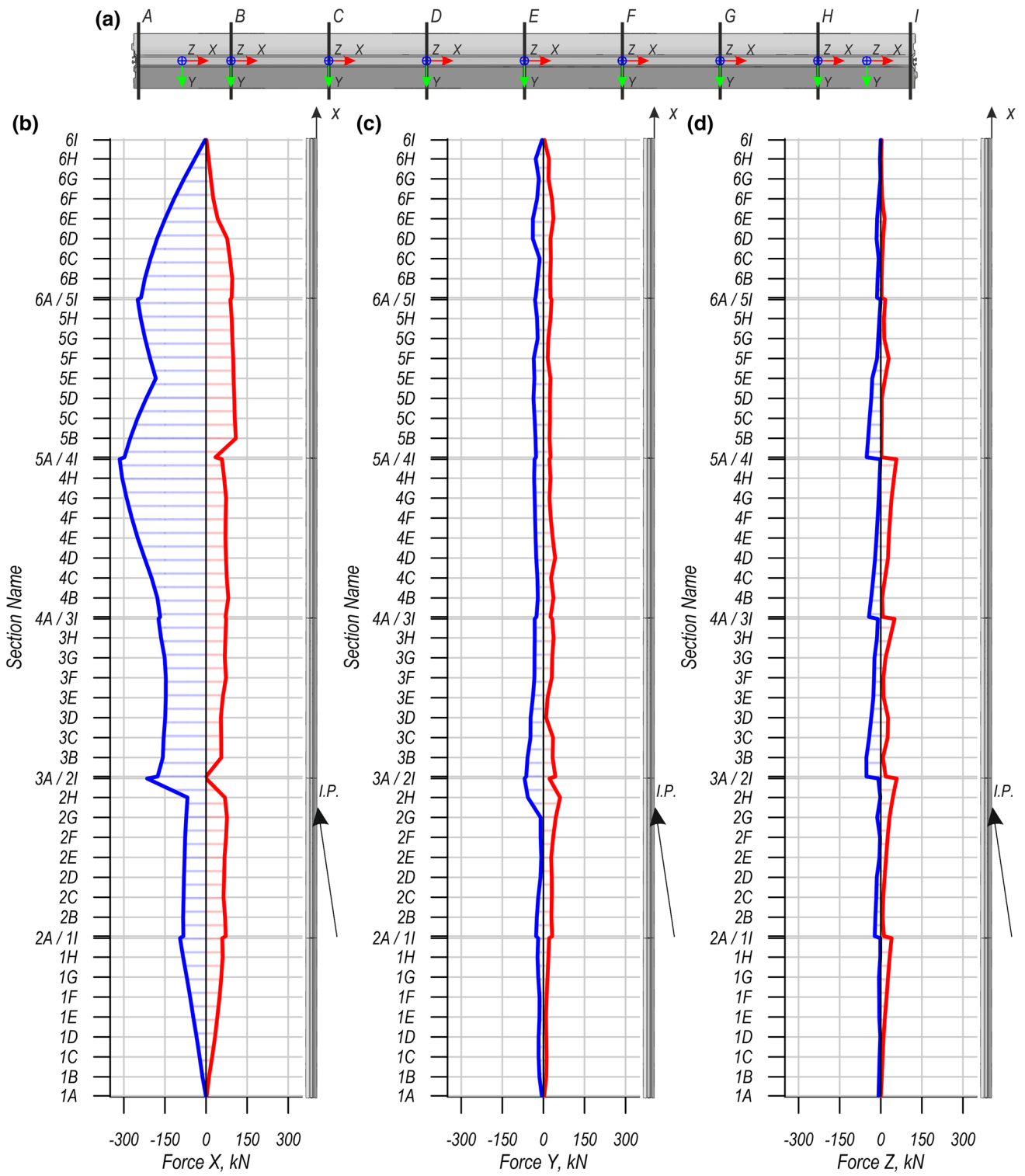
Fig. 14 Force envelopes for the H2/W5/B concrete road safety barrier obtained from the simulation results
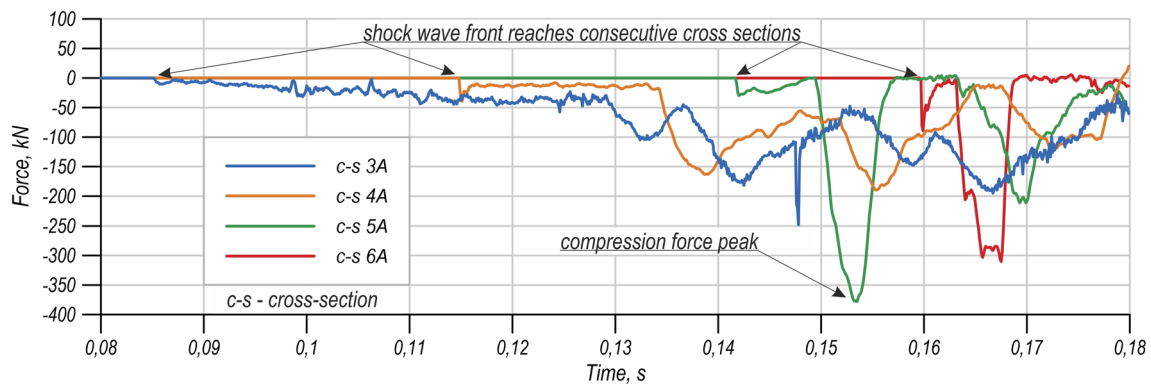
Fig. 15 Forces in cross sections 3A, 4A, 5A, and 6A as functions of time

3.2 Isolated segment analysis

The aforementioned forces were applied to the coupling part of the isolated segment, resulting in the transfer of stress to the reinforcement and surrounding concrete. In this section, the damage contours will be introduced. The damage shown in the figures represents the maximum between brittle and ductile damage, as mentioned in Sect. 2.2. The value of the damage parameter ranges from 0 (light gray), representing no damage, to 1 (black), representing complete damage. The plots were generated using the averaged element values. Note that the cracks seen in the photographs of the full-scale segments have been enhanced in the figures to facilitate comparison.

First, the full-scale segment damage and simulation damage results are paired in Fig. 19. In Fig. 19a, one can observe similar vertical and longitudinal cracks in both cases; however, the cracks from the numerical simulation are shorter. On the other hand, in Fig. 19b, the simulation results fail to capture the horizontal cracking observed in the real experiment. This might be due to the differences in load application, i.e., the intrusion of the HGV's wheel onto the segment (as occurred in the in situ test) was omitted. Figure 19c shows a similar horizontal curve that is also not found in the simulation results. However, both the full-scale crash test and the simulation results show longitudinal cracks that are characteristic of splitting failure phenomena [33, 34].

A general view of the damage isosurfaces is presented in Fig. 20a. This figure represents the isolated segment, where a white color means no damage, and colors from gray to black represent the value of the damage parameter. As one can observe, the concrete damage is located mainly near the coupling. According to the results of the numerical simulation, the area extending up to approximately 20 cm from the segment face has damage parameter values greater than 0. This portion is divided into sections to enable a detailed overview of this surface plot. The first cross section is located 2.1 cm from the segment's face, and the following 17 cross sections

are distributed every 1 cm. The numbering convention and dimensions are depicted in Fig. 20b. Detailed views of the aforementioned 18 cross sections are presented in Fig. 21. The initial plots contain the most severe damage, and the parameter contours diminish while moving farther from the segment's face. However, cross sections 11 and 12, near the end of the coupling part, also present relatively large areas of damage but with a lower magnitude. This might indicate that damage initiation occurs at the reinforcement. Thus, some of the cracks in real structures can remain unnoticed if they do not reach the outer surface. As the cross sections show, the vast majority of the damage is located on the impact side.

4 Conclusions

Improving road safety will always be a very significant issue. When it is impossible to ensure a sufficiently large safety zone or to remove obstacles near travel routes, road safety equipment, including safety barriers, can be used.

This paper presents an example of the TB41 crash test (10 t, 70 km/h, 8°) for a concrete barrier system. The tested barrier first contained the colliding truck and then properly redirected it back onto the road. A computational model of this crash event was developed, and the correctness of the calculations was verified on the basis of the full-scale test results.

The most important achievements of this paper include the following:

- A detailed description of concrete VRS modeling procedures.
- A list of modifications to the vehicle (10 t HGV) model.
- A validation against the TB41 full-scale crash test.
- The determination of the forces in the coupling region at the impact point.
- The creation of the force and moment envelopes.
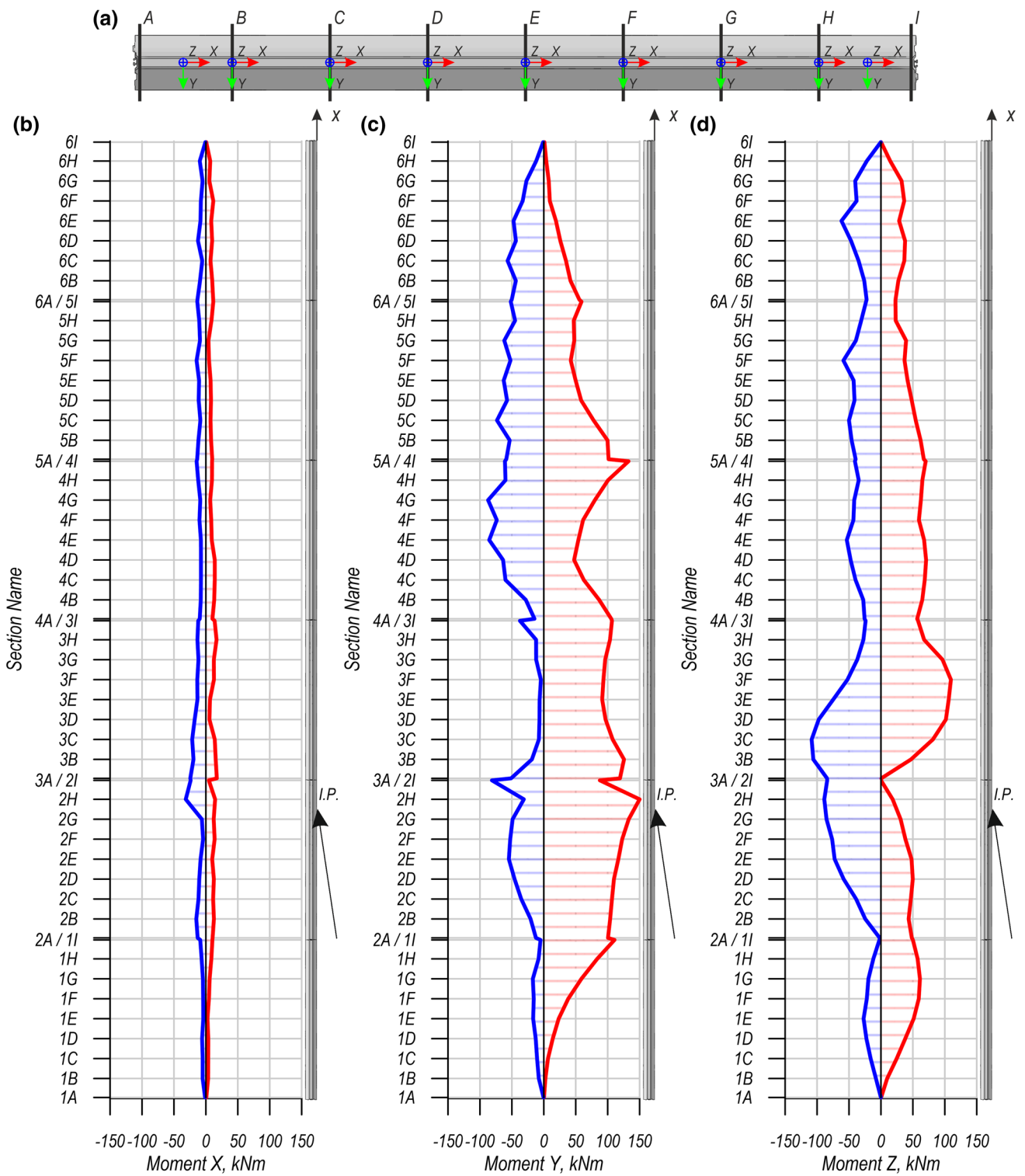- The successful reproduction of damage locations.

Fig. 16 Moment envelopes for the H2/W5/B concrete road safety barrier obtained from the simulation results
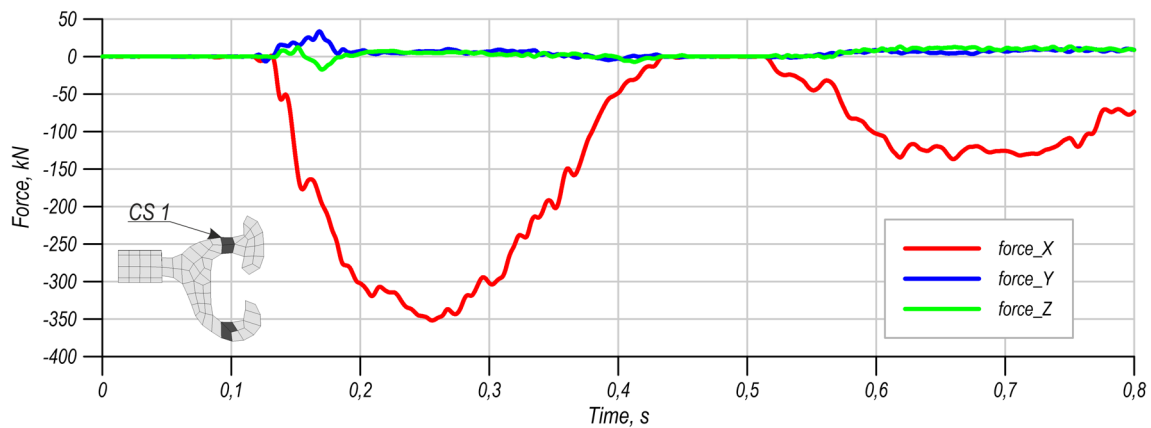
Fig. 17 Force curves from the coupling between segment no. 2 and segment no. 3, cross section CS 1
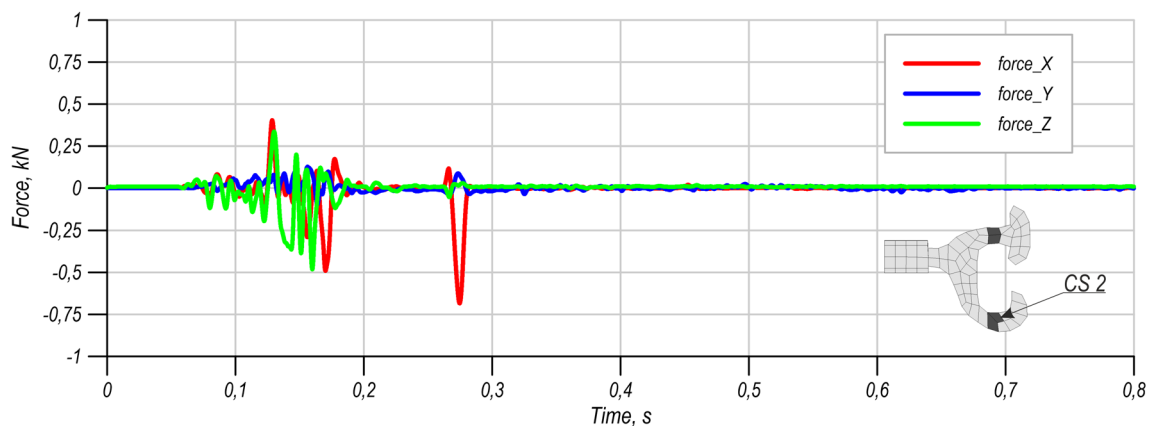

Fig. 18 Force curves from the coupling between segment no. 2 and segment no. 3, cross section CS 2

- A presentation of the detailed damage contours.

The most important findings and conclusions are listed below:

- Cracks in the concrete segments were found mostly near the coupling elements and reinforcement, not only near the impact point. Moreover, some cracks originating from the reinforcement may remain unnoticed if they do not reach the outer surface.
- Damage characteristic of splitting failure was found. Presumably, such longitudinal cracking may be alleviated by using an enhanced reinforcement design in the affected areas.
- The results from the numerical simulation show that the area near the reinforcement bars may be damaged after impact. More data will be needed to properly interpret

this result; however, it may mean that there are microcracks in this area.
- A high-frequency compression impulse running through the concrete barrier was found. It did not appear to be destructive in the TB41 test. However, the TB51 test could be investigated for a comparison of the results. Furthermore, the described barrier was a standalone system; boundary effects on the ends may lead to some higher force values.
- The HGV model proved to be sufficient for this application. However, if a more detailed analysis were to be carried out, the truck model could be a promising target of improvements. For example, the suspension breakage and tire blow-out could have influenced the energy dissipation of the impact.
- Bending in the Y–Z plane was found to be dominant, with the reinforcement connected to the coupling elements
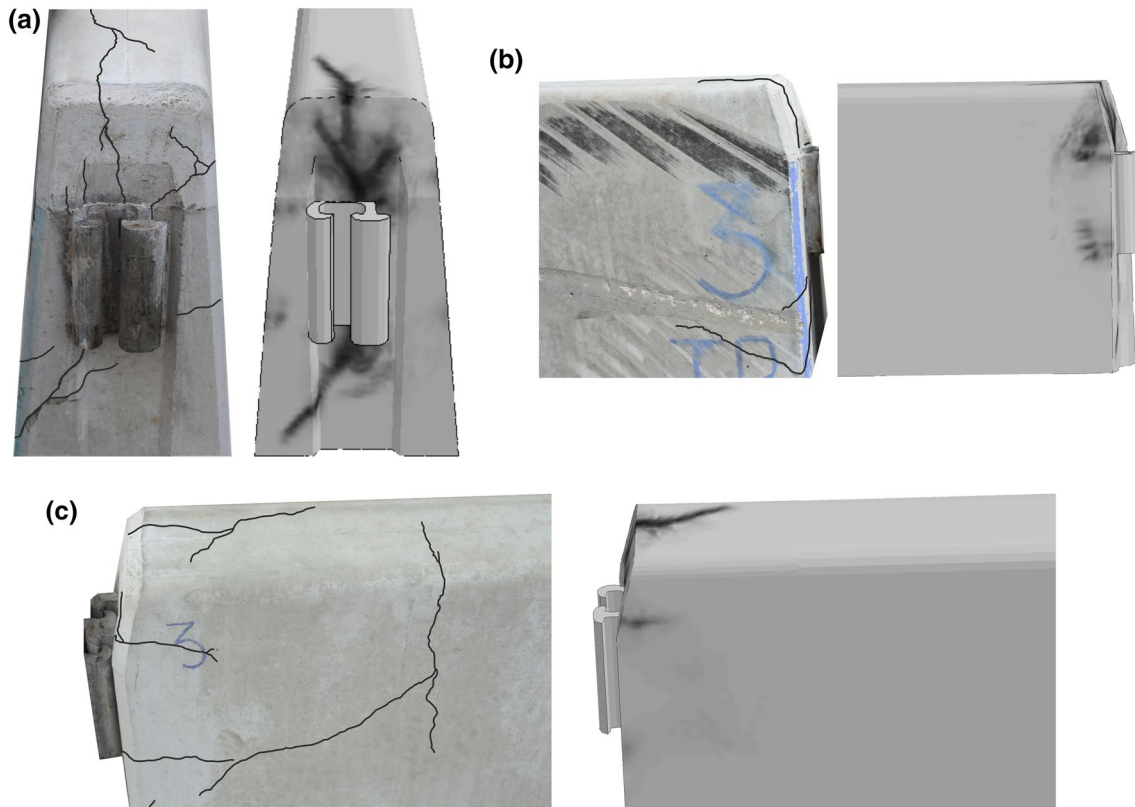
Fig. 19 Comparison of full-scale segment with enhanced cracks and simulated damage contour plots from different views: **a** coupling element view, **b** view from the impact side, and **c** view from the opposite side from the impact
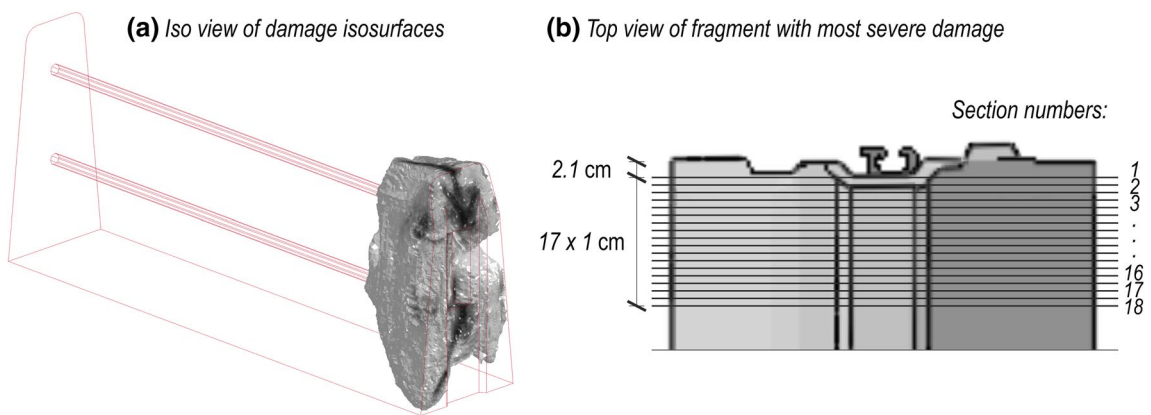

Fig. 20 Maximum of brittle and ductile damage results: **a** iso view and **b** top view and numbering convention

transferring tension and the concrete in the foot of each segment being mainly compressed. The next largest influence on the system appeared to be the bending in the X–Z plane. The obtained values may serve as guidelines for barrier section design.

Numerical simulations have proven to be a useful and valuable source of information. The developed model can

be successfully used in the future for further studies on road safety. Nevertheless, during the analysis of the results, a few questions arose. The answers may be sought by conducting further research in this area. These questions are as follows: How do the cracks near the reinforcing bars/coupling elements influence the function of the VRS? Can a concrete VRS sustain additional damage after a vehicle crash? Do all segments with cracks need to be replaced after a single impact?
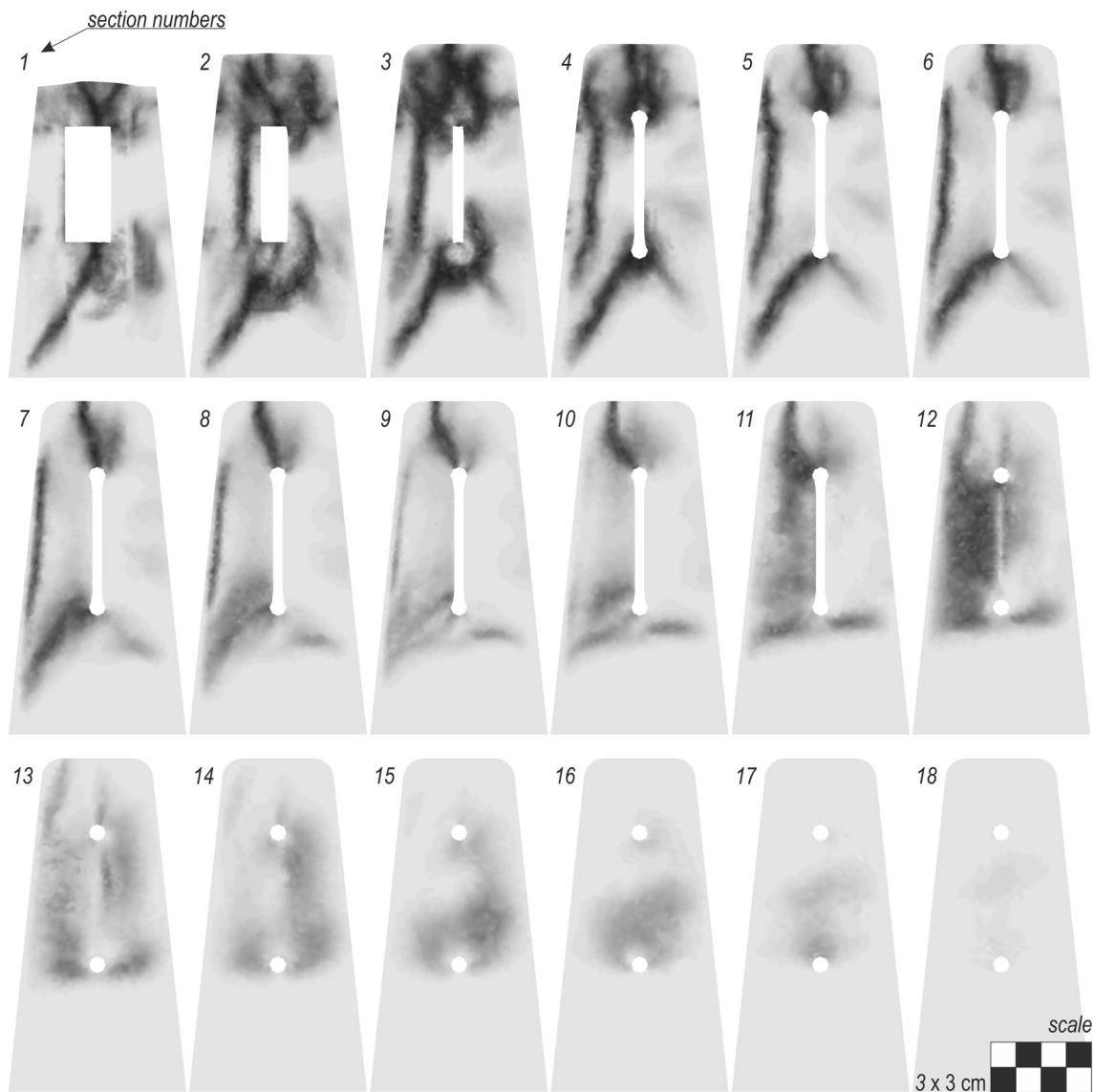
Fig. 21 Contours of the maximum of brittle and ductile damage in consecutive cross sections of the detailed isolated segment model

References

1. WHO. Global status report on road safety. 2018. https://www.who.int/publications-detail/global-status-report-on-roadsafety-2018.
2. Budzyński M, Wilde K, Jamroz K, Chróścielewski J, Witkowski W, Burzyński S, Bruski D, Jeliński Ł, Pachocki Ł. The effects of vehicle restraint systems on road safety. MATEC Web Conf. 2019;05003:1–8. https://doi.org/10.1051/matecconf/201926205003.
3. Budzyński M, Gobis A, Jamroz K, Jeliński Ł, Ostrowski K. Road restraint systems as a basis for roadside safety improvement.

IOP Conf Ser Mater Sci Eng. 2019;471:1–10. https://doi.org/10.1088/1757-899X/471/6/062029.

4. Budzyński M, Jamroz K, Jeliński Ł. Assessment of road restraint systems in Polish conditions. J KONBiN. 2018;45:325–43. https://doi.org/10.2478/jok-2018-0017.

5. European Standard EN 1317-1:2010. Road restraint systems – Part 1: terminology and general criteria for test methods, 2010.

6. European Standard EN 1317-2:2010. Road restraint systems – Part 2: performance classes, Impact test acceptance criteria and test methods for safety barriers including vehicle parapets, 2010.

7. Kuryłowicz-Cudowska A. Determination of thermophysical parameters involved in the numerical model to predict the temperature field of cast-in-place concrete bridge deck. Materials. 2019;12:3089. https://doi.org/10.3390/ma12193089.

8. Mikołajków L. Drogowe bariery ochronne betonowe Mag Autostrady. 2006;12:20–6.

9. Zain MFBM, Mohammed HJ. Concrete road barriers subjected to impact loads: an overview. Lat Am J Solids Struct. 2015;12:1824–58. https://doi.org/10.1590/1679-78251783.

10. NCHRP. Procedures for verification and validation of computer simulations used for roadside safety applications. 2011. https://doi.org/10.17226/17647.

11. Wekezer J, Oskard M, Logan R, Zywicz E. Vehicle impact simulation. J Transp Eng. 1993;199:598–617.

12. Wekezer JW, Kreja I, Issa M. Retrofit analysis of florida beam-and-post reinforced concrete bridge barriers. Eng. Trans. 2002;50:187–211.

13. Bonin G, Giuseppe C, Loprencipe G, Ranzo A. Road safety barriers with short elements of lightweight concrete. In: II International Congress SIIV—New Technology Modelling Tools Roads—Compend. Papers—27–29 Ottobre (2004).

14. Ren Z, Vesenjak M. Computational and experimental crash analysis of the road safety barrier. Eng Fail Anal. 2005;12:963–73. https://doi.org/10.1016/j.engfailanal.2004.12.033.

15. Borovinšek M, Vesenjak M, Ulbin M, Ren Z. Simulation of crash tests for high containment levels of road safety barriers. Eng Fail Anal. 2007;14:1711–8. https://doi.org/10.1016/j.engfailanal.2006.11.068.

16. Itoh Y, Liu C, Kusama R. Dynamic simulation of collisions of heavy high-speed trucks with concrete barriers. Chaos Solitons Fractals. 2007;34:1239–44. https://doi.org/10.1016/j.chaos.2006.05.059.

17. Borkowski W, Hryciów Z, Rybak P, Wysocki J. Testing the results of a passenger vehicle collision with a rigid barrier. J. KONES Powertrain Transp. 2010;17:1–7.

18. Borkowski W, Hryciów Z, Rybak P, Wysocki J. Numerical simulation of the standard TB11 and TB32 tests for a concrete safety barrier. J KONES Powertrain Transp. 2010;17:63–71.

19. Wang Q, Fang H, Li N, Weggel DC, Wen G. An efficient FE model of slender members for crash analysis of cable barriers. Eng Struct. 2013;52:240–56. https://doi.org/10.1016/j.engstruct.2013.02.027.

20. Li N, Fang H, Zhang C, Gutowski M, Palta E, Wang Q. A numerical study of occupant responses and injuries in vehicular crashes into roadside barriers based on finite element simulations. Adv Eng Softw. 2015;90:22–40. https://doi.org/10.1016/j.advengsoft.2015.06.004.

21. Abraham N, Ghosh B, Simms C, Thomson R, Amato G. Assessment of the impact speed and angle conditions for the EN1317 barrier tests. Int J Crashworthiness. 2016;21:211–21. https://doi.org/10.1080/13588265.2016.1164444.

22. Klasztorny M, Nycz DB, Szurgott P. Modelling and simulation of crash tests of N2-W4-A category safety road barrier in horizontal concave arc. Int J Crashworthiness. 2016;21:644–59. https://doi.org/10.1080/13588265.2016.1212962.

23. Klasztorny M, Zielonka K, Nycz DB, Posuniak P, Romanowski RK. Experimental validation of simulated TB32 crash tests for SP-05/2 barrier on horizontal concave arc without and with composite overlay. Arch Civ Mech Eng. 2018;18:339–55. https://doi.org/10.1016/j.acme.2017.07.007.

24. Mohan M, Canceri J, Jackson J. Simulating barrier crashworthiness with high certainty and ensuring safety in design, 10th Austroads Bridge Conference in Melbourne, 2017.

25. Yin H, Fang H, Wang Q, Wen G. Design optimization of a MASH TL-3 concrete barrier using RBF-based metamodels and nonlinear finite element simulations. Eng Struct. 2016;114:122–34. https://doi.org/10.1016/j.engstruct.2016.02.009.

26. Yin H, Xiao Y, Wen G, Fang H. Design optimization of a new W-beam guardrail for enhanced highway safety performance. Adv Eng Softw. 2017;112:154–64.

27. Wang Q, Fang H, Yin H. A probability-based approach for assessment of concrete median barriers. In: International Conference on Transport Development. 2018;171–9.

28. Wilde K, Jamroz K, Bruski D, Budzyński M, Burzyński S, Chróścielewski J, Witkowski W. Curb-to-barrier face distance variation in a TB51 bridge barrier crash test simulation. Arch Civ Eng. 2017;63:187–99.

29. PD CEN/TR 16303-1:2012. Road restraint systems—guidelines for computational mechanics of crash testing against vehicle restraint system. Part 1: common reference information and reporting. 2012.

30. PD CEN/TR 16303-2:2012. Road restraint systems—guidelines for computational mechanics of crash testing against vehicle restraint system. Part 2: vehicle modelling and verification. 2012.

31. PD CEN/TR 16303-3:2012. Road restraint systems—guidelines for computational mechanics of crash testing against vehicle restraint system. Part 3: test item modelling and verification. 2012.

32. PD CEN/TR 16303-4:2012. Road restraint systems—guidelines for computational mechanics of crash testing against vehicle restraint system. Part 4: validation procedures. 2012.

33. Gálvez JC, Benítez JM, Tork B, Casati MJ, Cendón DA. Splitting failure of precast prestressed concrete during the release of the prestressing force. Eng Fail Anal. 2009;16:2618–34. https://doi.org/10.1016/j.engfailanal.2009.04.023.

34. Rucka M, Wilde K. Experimental study on ultrasonic monitoring of splitting failure in reinforced concrete. J Nondestruct Eval. 2013;32:372–83. https://doi.org/10.1007/s10921-013-0191-y.

35. Mohammed HJ, Zain MFBM. Simulation assessment and theoretical verification of a new design for portable concrete barriers. KSCE J Civ Eng. 2017;21:851–62. https://doi.org/10.1007/s12205-016-0603-5.

36. Wekezer JW, Kreja I, Gilbert C. Conceptual analysis of an aesthetic bridge barrier. Report (1997).

37. Murray Y. Users manual for LS-DYNA concrete material model 159. 2007.

38. Murray Y, Abu-Odeh A, Bligh R. Evaluation of LS-DYNA concrete material model 159. 2007.

39. Hallquist JO. LS-DYNA theory manual. 2006;680.

40. LSTC, LS-DYNA R8.0 keyword user's manual. 2015.

41. Jiang H, Zhao J. Calibration of the continuous surface cap model for concrete. Finite Elem Anal Des. 2015;97:1–19. https://doi.org/10.1016/j.finel.2014.12.002.

42. Bielenberg RW, Faller RK, Quinn TE, Sicking DL, Reid JD. Development of a retrofit low-deflection. Temporary Concrete Barrier System. 2014.

43. Agrawal AK, Xu X. Finite element simulation of truck impacts on highway bridge piers. 2016. https://doi.org/10.1007/bf02481509.

44. Zhou D, Li R, Wang J, Guo C. Study on impact behavior and impact force of bridge pier subjected to vehicle collision. Shock Vib. 2017;2017:1–12. https://doi.org/10.1155/2017/7085392.

45. Miśkiewicz M, Bruski D, Chróścielewski J, Wilde K. Safety assessment of a concrete viaduct damaged by vehicle impact and an evaluation of the repair. Eng Fail Anal. 2019;106:104147. https://doi.org/10.1016/j.engfailanal.2019.104147.

46. Cowper GR, Symonds PS. Strain hardening and strain-rate effects in the impact loading of cantilever beams. Report no. 28. 1957.

47. Wu W, Thomson R. A study of the interaction between a guardrail post and soil during quasi-static and dynamic loading. Int J Impact Eng. 2007;34:883–98. https://doi.org/10.1016/j.ijimpeng.2006.04.004.

48. Pachocki Ł, Wilde K. Numerical simulation of the influence of the selected factors on the performance of a concrete road barrier H2/W5/B. MATEC Web Conf. 2018;01014:1–9. https://doi.org/10.1051/matecconf/201823101014.

49. Pachocki Ł, Bruski D, Burzyński S, Chróścielewski J, Wilde K, Witkowski W. On the influence of the acceleration recording time on the calculation of impact severity indexes. MATEC Web Conf. 2018;03010:1–8. https://doi.org/10.1051/matecconf/201821903010.

50. Wilde K, Bruski D, Burzyński S, Chróścielewski J, Pachocki Ł. LS-DYNA simulations of the impacts of a 38-ton heavy goods vehicle into a road cable barrier. In: 12th European LS-DYNA conference. 2019. p. 20–2.

51. Reid JD, Boesch DA, Bielenberg RW. Detailed tire modeling for crash applications. Int J Crashworthiness. 2007;12:521–9. https://doi.org/10.1080/13588260701483813.

52. Baranowski P, Malachowski J, Janiszewski J, Wekezer J. Detailed tyre FE modelling with multistage validation for dynamic analysis. Mater Des. 2016;96:68–79. https://doi.org/10.1016/j.matdes.2016.02.029.

53. Gutowski M, Palta E, Fang H. Crash analysis and evaluation of vehicular impacts on W-beam guardrails placed behind curbs using finite element simulations. Adv Eng Softw. 2017;114:85–97.

54. Avallone EA, Baumeister III T, Sadegh AM. Marks' standard handbook for mechanical engineers. 2006.

55. Plaxico CA, Kennedy JC, Miele CR. Development of an NCHRP Report 350 TL-3 New Jersey shape 50-inch portable concrete barrier. 2006.

56. Mongiardini M, Ray MH. Acceptance criteria for validation metrics in roadside safety based on repeated full-scale crash tests. Int J Reliab Saf. 2010;4:69–88.

57. Mongiardini M, Ray MMH, Anghileri M, Milano P. Development of a software for the comparison of curves during the verification and validation of numerical models. In: 7th European LS-DYNA. 2009. http://www.dynamore.de/de/download/papers/papers/konferenz09/papers-depr/K-I-03.pdf.

58. Bruski D, Burzyński S, Chróścielewski J, Jamroz K, Pachocki Ł, Witkowski W, Wilde K. Experimental and numerical analysis of the modified TB32 crash tests of the cable barrier system. Eng Fail Anal. 2019;104:227–46. https://doi.org/10.1016/j.engfailanal.2019.05.023.

59. Wilde K, Bruski D, Budzyński M, Burzyński S, Chróścielewski J, Jamroz K, Pachocki Ł, Witkowski W. Numerical analysis of TB32 crash tests for 4-cable guardrail barrier system installed on the horizontal convex curves of road (in press). Simul: Int J Nonlinear Sci Numer; 2018.

60. European Standard EN 1317-4:2001. Road restraint systems - Part 4: performance classes, impact test acceptance criteria and test methods for terminals and transitions of safety barriers, 2001.

Springer